

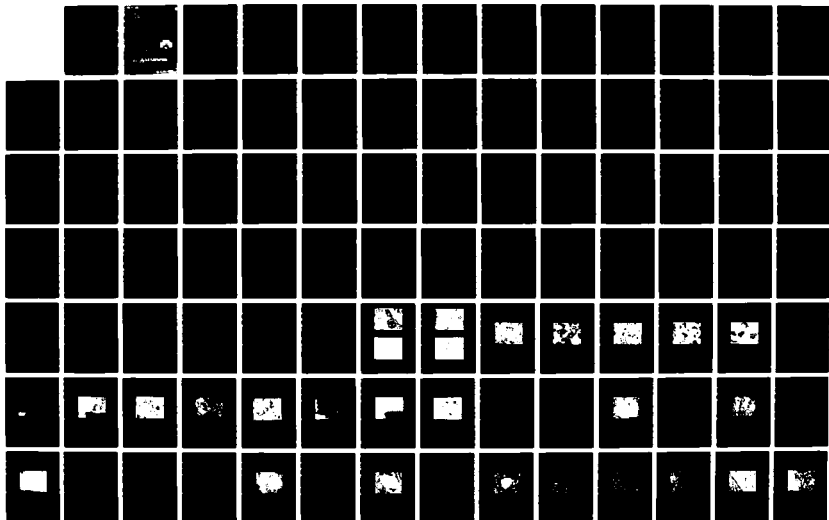
AD-A193 939

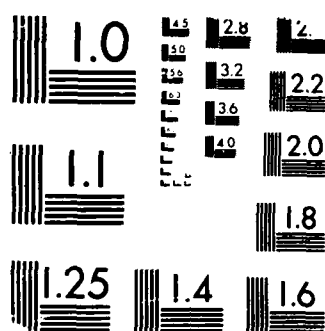
PLASMA JOINING OF METAL MATRIX COMPOSITES(U) MSNM INC
SAN MARCOS CA G H REYNOLDS ET AL. 25 FEB 88
ARO-22817. 0-HS-5 DAAG29-85-C-0027

1/2

UNCLASSIFIED

F/G 11/6.2 NL





MICROCOPY RESOLUTION TEST CHART
NBS 1963-A

AD-A193 939

MEMU, INC.

1000 E. 10th St.
 San Mateo, California 94403
 (415) 744-1000

PLASMA JOINING OF METAL MATRIX COMPOSITES

Final Report

Prepared by G. H. Reynolds and L. Wang MEMU, Inc.

February 1988

U.S. Army Research Office

Contract No. DAAH04-80-1-0001

Approved for Public Release

TABLE OF CONTENTS

EXECUTIVE SUMMARY.....	1
1.0 MODELING STUDIES.....	6
2.0 COMPOSITE POWDER PREPARATION AND EVALUATION.....	7
3.0 LOW-PRESSURE PLASMA DEPOSITION.....	29
4.0 MECHANICAL TESTING.....	40
5.0 REFERENCES.....	42

Accession For	
NTIS GRA&I	<input checked="" type="checkbox"/>
DTIC TAB	<input type="checkbox"/>
Unannounced	<input type="checkbox"/>
Justification	
By	
Distribution/	
Availability Codes	
Dist	Avail and/or Special
A-1	DTIC COP INSPC

UNCLASSIFIED

SECURITY CLASSIFICATION OF THIS PAGE

REPORT DOCUMENTATION PAGE

1a. REPORT SECURITY CLASSIFICATION Unclassified			1b. RESTRICTIVE MARKINGS		
2a. SECURITY CLASSIFICATION AUTHORITY			3. DISTRIBUTION / AVAILABILITY OF REPORT Approved for public release; distribution unlimited.		
2b. DECLASSIFICATION / DOWNGRADING SCHEDULE					
4. PERFORMING ORGANIZATION REPORT NUMBER(S)			5. MONITORING ORGANIZATION REPORT NUMBER(S) ARO 22817.8-MS-5		
6a. NAME OF PERFORMING ORGANIZATION MSNW, Inc.		6b. OFFICE SYMBOL (if applicable)	7a. NAME OF MONITORING ORGANIZATION U. S. Army Research Office		
6c. ADDRESS (City, State, and ZIP Code) P. O. Box 865 San Marcos CA 92069			7b. ADDRESS (City, State, and ZIP Code) P. O. Box 12211 Research Triangle Park, NC 27709-2211		
8a. NAME OF FUNDING / SPONSORING ORGANIZATION U. S. Army Research Office		8b. OFFICE SYMBOL (if applicable)	9. PROCUREMENT INSTRUMENT IDENTIFICATION NUMBER DAAG29-85-C-0027		
8c. ADDRESS (City, State, and ZIP Code) P. O. Box 12211 Research Triangle Park, NC 27709-2211			10. SOURCE OF FUNDING NUMBERS	PROGRAM ELEMENT NO.	PROJECT NO.
			TASK NO.	WORK UNIT ACCESSION NO.	
11. TITLE (Include Security Classification) Plasma Joining of Metal Matrix Composites					
12. PERSONAL AUTHOR(S) L. Yang and G. H. Reynolds					
13a. TYPE OF REPORT Final		13b. TIME COVERED FROM Sept 1985 TO Oct 1987		14. DATE OF REPORT (Year, Month, Day) February 25, 1988	
15. PAGE COUNT 99					
16. SUPPLEMENTARY NOTATION The view, opinions and/or findings contained in this report are those of the author(s) and should not be construed as an official Department of the Army position, policy, or decision, unless so designated by other documentation.					
17. COSATI CODES			18. SUBJECT TERMS (Continue on reverse if necessary and identify by block number)		
FIELD	GROUP	SUB-GROUP	Metal matrix composites, Joining, Plasma processing		
19. ABSTRACT (Continue on reverse if necessary and identify by block number) This project was an analytical and experimental investigation of low pressure, transferred arc plasma joining of discontinuously reinforced metal matrix composites using composite powder filler metals. Modeling of the expected effects of plasma processing on the composite powder filler metals was performed. Microstructural and microchemical characterizations were performed on plasma processed composite powder filler metals, composite deposits produced on inert substrates, and composite weld metal emplaced in butt joints in 6061 - 30 wt.% SiC _p base plates. Similar characterizations were performed on fusion line and heat affected zone regions of the composite weldments. Preliminary measurements of weldment mechanical properties (joint efficiency) were performed.					
20. DISTRIBUTION / AVAILABILITY OF ABSTRACT <input type="checkbox"/> UNCLASSIFIED/UNLIMITED <input type="checkbox"/> SAME AS RPT. <input type="checkbox"/> DTIC USERS			21. ABSTRACT SECURITY CLASSIFICATION Unclassified		
22a. NAME OF RESPONSIBLE INDIVIDUAL			22b. TELEPHONE (Include Area Code)		22c. OFFICE SYMBOL

EXECUTIVE SUMMARY

The project was an investigation of plasma processing of model metal matrix composite powders, use of same as filler metals for plasma joining of metal matrix composites, and modeling of the relevant thermochemical and thermophysical phenomena underlying plasma processing, plasma deposition and structure/property evolution in plasma deposited composite weld metals.

Initial modeling studies on the composite powders have treated matrix alloy and alloying element vaporization loss in-plasma and reinforcing phase vaporization loss in-plasma. Using available thermochemical data these effects have been shown to be minor under realistic processing conditions. Thermal stability of surface oxide films in-plasma has been found to be such that film losses on the order of a monolayer of Al_2O_3 are predicted during plasma processing. Similarly, it has been shown that dissolved hydrogen removal from composite droplets in-plasma would be expected to be nearly complete under realistic plasma processing conditions.

Modeling studies of the effect of low pressure plasma processing on the composite powders may be summarized as follows:

1. Loss of Al matrix material by evaporation is less than 10% even at 2300°K if the residence time in-plasma is less than 10^{-3} seconds.
2. Losses of (1) Zr or Ti alloying elements, (2) SiC, ZrC and TiC dispersed phases, and (3) Al_2O_3 surface film on the Al matrix, are negligible at 2300°K for in-plasma residence times as long as 10^{-2} seconds.

3. Significant amounts of hydrogen dissolved in the Al matrix are lost at the melting point of Al if the residence time in-plasma is longer than 10^{-3} seconds. The presence of an oxide film on the surface of the molten droplets does not impede the removal of hydrogen from the droplet surface.

4. SiC will react with the Al matrix to form Al_4C_3 . Loss of SiC by such reaction is about 10% at $2300^{\circ}K$ for in-plasma residence time of 10^{-3} seconds, if the rate limiting factor is the diffusion of the product Si into the molten Al matrix.

5. Zr and Ti alloying additions to the Al matrix will react with SiC to form ZrC and TiC, which are stable toward Al. For the highest Zr and Ti alloy concentrations used in this study (3 wt. % Zr and 5 wt. % Ti), the maximum thicknesses of ZrC and TiC formed during plasma processing of a model composite, containing alternate layers of SiC and Al of 10 microns thickness each, are 0.07 micron and 0.17 micron, respectively.

Composite Al-SiC powders were prepared having 1100 (commercially pure) aluminum, aluminum - 3 wt.% zirconium or aluminum - 5 wt. % titanium alloy matrices with 30 wt. % uniformly dispersed silicon carbide particulate reinforcing phase. The composite powders were extensively characterized in the as-produced condition for determination of the effects of plasma processing. Low pressure plasma deposits of each model composite system were successfully produced both with and without the presence of a transferred arc during deposition. Low pressure plasma processed composite powders allowed to solidify in transit without impingement on a substrate were also prepared.

Composite weld metal deposits were also produced in butt joints in 6061 aluminum - 30 wt. % SiC_p composite base plates and evaluated for comparison to the as-produced composite powders used as feed materials.

Low pressure, transferred arc plasma processing was found to cause a general reduction in composite powder particle size and in the size of the SiC particulate phase dispersed within the composite powder particles. Alloy matrices containing reactive metal additions show an increase in reactive metal concentration near the matrix/reinforcing phase interface which is expected since reactive metal carbides (TiC , ZrC) are expected to form preferentially at the interface. This effect is desirable to prevent interfacial Al_4C_3 formation during plasma processing. Loss of some of SiC during processing of the 1100 aluminum - 30 wt.% SiC_p composite powders has been observed. This effect, which may be preceded by Al_4C_3 formation, is apparently suppressed in matrix alloys containing reactive metal additions. All observations are in basic agreement with the predictions of the thermochemical modeling studies performed to anticipate interfacial chemical reactions which might occur during plasma processing of each of the model alloys.

Deposits produced on inert substrates show, due to their slower cooling rates compared to powders allowed to solidify in free flight, more pronounced reactive metal concentration build-up at the particle/matrix interface and discrete reactive metal-rich phases (such as Al_3Ti and Al_3Zr) in the matrix alloy. Fragmentation of the dispersed SiC phase described above is also noted in solid deposited material. The deposits contain a uniform dispersion of the SiC reinforcing phase in each alloy matrix type.

An important objective of the project was optimization of deposit/substrate, i.e. fusion line, bond strength for maximum joint efficiency. Significant progress was made by utilizing deposition at relatively high transferred arc intensities for maximum substrate surface melting and maximum bonding of the deposited composite weld metal. It was shown possible to produce uniformly reinforced composite weld metal, metallurgically bonded to composite base plates, by the low pressure, transferred arc plasma deposition process.

Microstructural and microchemical changes occurring at the fusion line and in the heat affected zone of Al/SiC_p composites welded using a low pressure, transferred arc plasma process with composite powder filler metals were also determined. Of particular interest were the formation of an apparent SiC particle-free zone at the fusion line of some welds, particularly those produced using an 1100 aluminum - 30 wt.% SiC_p composite filler metal, and possible matrix/reinforcing phase interfacial chemical reactions in the heat affected zone microstructure. It has been found that the "particle-free" fusion line microstructural zone is actually reinforced by very fine SiC particulates which apparently formed by disintegration of the starting SiC particulates in the base metal, in the composite powder filler metal, or in both. The width of this zone is considerably less or the zone is absent entirely when the filler metal matrix composition contains a small amount of either Ti or Zr. Also, a similar microstructure occurs in isolated zones dispersed in the deposited composite weld metal only for the 1100 aluminum - 30 wt.% SiC_p weld metal. This suggests that the extent of interfacial reactions during plasma processing, which should be greatest in the 1100 aluminum matrix alloy composition, affects the degree of SiC particulate disintegration in the

deposited weld metal and at the fusion line. Since the fusion line microstructure is reinforced, at least by small SiC particles in the worst case and by large SiC particles in most cases, the effect of this zone on as-welded mechanical properties will receive particular attention in the future. No conclusive evidence of matrix/reinforcing phase of interfacial reactions was found in the heat-affected zone of the Al/SiC_p base material, as expected in a relatively low heat input joining process such as the one under study.

Initial mechanical property test results should fracture occurring in the weld metal by intervoid linkage. The strength of the bond line could not be determined because of preferential fracture in the weld metal. The optimization of as-welded mechanical properties will require plasma deposition process optimization to reduce levels of weld metal porosity.

1.0 MODELING STUDIES

Some of the physical and chemical events occurring during plasma processing of composite powders which may affect the structure and properties of the deposit have been analyzed on the basis of thermodynamic and kinetic considerations. The results are described in the following sections.

1. Loss of Al Alloy Matrix by Vaporization in the Plasma.

Assuming the surface of the spherical Al droplets is clean and at a temperature of $T^{\circ}\text{K}$, the fractional loss of droplet radius $\Delta r/r$ by vaporization in a time period of t seconds, can be expressed as:

$$\frac{\Delta r}{r} = \frac{\alpha p t}{\rho r} \left(\frac{M}{2\pi R T} \right)^{1/2} \quad (1)$$

where α = vaporization coefficient ()

p = vapor pressure of Al in dynes/cm² at $T^{\circ}\text{K}$

ρ = density of Al (2.7 g/cm³)

r = radius of Al droplets in cm.

R = gas constant (8.31×10^7 ergs/ $^{\circ}\text{K}$ /mole)

M = atomic weight of Al (27 g/mole)

Substituting ρ, R , and M into equation (1) we obtain:

$$\frac{\Delta r}{r} = 8.42 \times 10^{-5} \frac{\alpha p t}{(T)^{1/2} r} \quad (2)$$

Calculations of $\Delta r/r$ are performed for the following conditions:

$T = 950, 1080, 1245, 1480, 1820, 2350^{\circ}\text{K}$,

$t = 10^{-2}, 10^{-3}, 10^{-4}$ seconds, and

$r = 75, 22$ microns.

These values are selected in anticipation of the ranges of the plasma deposition process parameters to be used in the experimental portion of the program. α , the evaporation coefficient, is assumed to be unity since this represents the worst case from the point of view of evaporation loss. The calculated results are shown in Table 1. It can be seen that the loss of Al alloy matrix material becomes significant only when the temperature reaches 2350°K and the residence time in plasma exceeds 10^{-3} seconds.

At 2350°K , the decrease in droplet radius is less than about 10% even for droplets of 22 microns radius if the time of residence in the plasma can be kept below 10^{-3} seconds. For a working distance of 0.3 meter and a droplet velocity of Mach 1 (332 meter/second), the residence time of the droplets in the plasma should be less than 10^{-3} seconds. For droplet velocities higher than Mach 1, the residence time will be even shorter. Furthermore, since the vaporization coefficient is usually less than unity, the actual vaporization loss should be less than that shown in Table 1. The loss of Al alloy matrix material by evaporation in the plasma therefore does not appear to be a significant problem during plasma deposition processing.

2. Loss Of Alloying Elements By Vaporization In Plasma

Alloying elements in the Al matrix, such as Zr, Ti, or B, can be lost by selective vaporization in the plasma. Assuming the concentration of the alloying element is low (less than a few mole percent) and that the alloying element forms an ideal solution with Al, the number of atoms of the alloying element lost by vaporization $-dn_x$, in time dt from the Al alloy droplet can be expressed as:

$$-dn_x = \frac{\alpha p_x x}{(2\pi m_x kT)^{1/2}} 4\pi r^2 \cdot dt \quad (3)$$

where:

- α = vaporization coefficient for the alloying element,
- p_x = vapor pressure of the alloying element at temperature T ,
- x = mole fraction of the alloying element in Al,
- r = radius of the Al droplet,
- m_x = weight of the atom of the alloying element, and
- k = Boltzmann constant

For dilute solutions:

$$x = \frac{n_x}{n_{Al}} \quad (4)$$

and

$$n_{Al} = \frac{4}{3} \pi r^3 \rho_{Al} \frac{N_o}{M_{Al}} \quad (5)$$

where:

n_x = number of atoms of the alloying element in the Al alloy droplet,

n_{Al} = number of atoms of Al in the Al alloy droplet

ρ_{Al} = density of Al (2.7 g/cc)

M_{Al} = atomic weight of Al (27 g/mole)

N_0 = Avogadro's Number (6.1×10^{23} /mole)

Substituting Equations (4) and (5) into Equation (3), we obtain:

$$-\frac{dn_x}{n_x} = 1.31 \times 10^{-3} \frac{\alpha p_x}{r(M_x T)^{1/2}} \cdot dt \quad (6)$$

where M_x = atomic weight of the alloying element. If r is not a function of time and α is taken as unity, Equation (6) can be integrated to give:

$$n_x = n_x^0 \exp \left(- \frac{1.31 \times 10^{-3} p_x t}{r(M_x T)^{1/2}} \right) \quad (7)$$

where n_x = number of atoms of the alloying element in the Al droplet after time t in the plasma, and n_x^0 = number of atoms of the alloying element in the Al droplet at $t = 0$.

Equation (7) is used to calculate n_x for Zr ($M_x = 91.22$) in an Al alloy droplet of radius equal to 22×10^{-4} cm after 10^{-3} second at 2275 °K. At 2275 °K, $p_{Zr} =$

0.133 dynes/cm²; therefore:

$$n_x = {}^o n_x \exp \left(- \frac{1.31 \times 10^{-3} \times 0.133 \times 10^{-3}}{22 \times 10^{-4} (91.22 \times 2275)^{1/2}} \right) \approx {}^o n_x$$

Thus the loss of Zr from the Al alloy droplet is negligible. Similar conclusions are reached for Ti and B alloying additions in the Al alloy droplet under these conditions. Therefore the loss of these alloying elements from Al alloy droplets during their residence time in plasma does not seem to be a significant problem even at high temperatures and for relatively long residence times (10^{-3} seconds) in the plasma. The above calculations assume that the alloying element forms an ideal solution with Al. Zr, Ti, and B, however, all form intermetallic compounds with Al, indicating strong affinity between these elements and Al. Vaporization losses should therefore be even lower than those calculated on the basis of an ideal solution.

3. Loss Of The Dispersed Reinforcing Phases (SiC, ZrC or TiC) In Plasma.

SiC, ZrC and TiC dissociate at high temperatures according to the equations:



and the dissociation products may be lost by condensation in the cooler part of the system. To assess the magnitude of such loss, calculations can be made for the loss of these materials at 2300°K for a residence time of 10^{-2} seconds in the plasma.

On the basis of thermodynamic data available [Reference (2)], the equilibrium vapor pressures of Si, Zr, and Ti for reactions (8), (9), and (10) at 2300°K are calculated by using the equation:

$$\Delta F^0 = -RT \ln p^2 \quad (11)$$

where ΔF^0 is the standard free energy change for the reaction at temperature T, R is the gas constant, and p is the equilibrium vapor pressure of Si, Zr, or Ti over the respective carbide. At 2300°K, $p_{Si} = 1.07 \times 10^{-6}$ atm, $p_{Zr} = 3.81 \times 10^{-10}$ atm., and $p_{Ti} = 1.47 \times 10^{-8}$ atm. Assuming a vaporization coefficient of unity, the loss of the thickness of carbide in time t can be calculated from these vapor pressure values by the equation:

$$\Delta l = \frac{p_x}{\rho_{MC}} \left(\frac{M_x}{2\pi RT} \right)^{1/2} \frac{M_{MC}}{M_x} \cdot t \quad (12)$$

where:

Δl = loss of thickness of carbide in cm,

p_x = vapor pressure of Si, Zr, or Ti in dynes/cm²,

ρ_{MC} = density of carbide ($\rho_{SiC} = 3.20$ g/cm³, $\rho_{ZrC} = 6.70$ g/cm³,
 $\rho_{TiC} = 4.25$ g/cm³)

R = gas constant (8.31×10^7 erg/°K/mole),

T = temperature in $^{\circ}\text{K}$,
 M_{MC} = molecular weight of carbide,
 M_x = atomic weight of Si, Zr, or Ti,
 t = time in seconds

Using Equation (12) and the vapor pressures of Si, Zr, and Ti calculated from Equation (11), Δl values for $T = 2300^{\circ}\text{K}$, and $t = 10^{-2}$ seconds are found to be:
 $\Delta l_{\text{SiC}} = 2.34 \times 10^{-8} \text{ cm}$, $\Delta l_{\text{ZrC}} = 2.39 \times 10^{-12} \text{ cm}$, and
 $\Delta l_{\text{TiC}} = 2.77 \times 10^{-10} \text{ cm}$.

Thus the loss of these carbide reinforcing phase is negligible even at high temperatures (2300°K) and relatively long residence times (10^{-2} seconds). Therefore the loss of the carbide reinforcing phase during plasma processing of precomposited powders does not appear to be a significant problem.

4. Stability of the Oxide Film On The Surface Of Al Alloy Droplets In Plasma.

The precomposited Al alloy powders, like any Al powders used for the fabrication of Al matrix composites, are expected to have a surface film of Al_2O_3 . Whether this surface oxide film is stable in the plasma during plasma deposition is of great interest since this oxide film may impede the adhesion between particles in the deposited composite microstructure. It may have to be broken up by mechanical working of the deposit in order to achieve optimum mechanical properties.

The removal of the oxide surface film by vaporization has been evaluated according to the following two mechanisms



or,



The standard free energy of reaction is deduced from free energy data given in Reference (3).

For Equation (13) $\Delta F^\circ = 357,410 - 92.16 T$ calories per mole

For Equation (14) $\Delta F^\circ = 411,700 - 106.15 T$ calories per mole

The equilibrium pressures of Al_2O_3 and AlO are calculated for various temperatures by using these ΔF° values assuming no oxygen contamination in the carrier gas. The results are shown in Table 2.

It can be seen that Equation (14) yields a higher dissociation pressure than Equation (13). However, the rate of removal of the Al_2O_3 surface film according to Equation (14) is still not high enough to lead to appreciable cleaning of the droplet surface. At 2300°K and for a residence time as long as 10^{-2} seconds in the plasma, the loss of thickness of the Al_2O_3 surface film, calculated by using $p_{\text{AlO}} = 5.55 \times 10^{-7}$ atm. and an equation similar to Equation (12), is only 1.02×10^{-8} cm. Since the carrier gas usually contains some oxygen impurities, the loss of the surface Al_2O_3 film should therefore be even lower than this value.

5. Removal Of Hydrogen From The Al Matrix During Heating In Plasma

It would be extremely useful if the hydrogen present in the Al alloy matrix could be removed during heating in the plasma. The Al matrix alloy powder can contain as much as several ppm of hydrogen which can cause porosity in the consolidated products. The loss of hydrogen from the molten Al alloy droplet during residence in the plasma is calculated by using the following equation [Reference (4)] assuming zero concentration of hydrogen at the surface of the droplet because of the rapid removal of the surface hydrogen atoms by the carrier gas.

$$F = 1 - \frac{6}{\pi^2} \sum_{n=1}^{\infty} \frac{1}{n^2} \exp \left(- \frac{n^2 \pi^2 D t}{r^2} \right) \quad (15)$$

where:

F = fractional loss of hydrogen from the Al alloy droplet,

D = diffusivity of hydrogen in aluminum in cm^2/sec ,

t = time of diffusion in seconds,

r = radius of the Al alloy droplet in cm.

F values have been calculated for an Al droplet at its melting point

($D = 7.6 \times 10^{-4} \text{ cm}^2/\text{sec}$., Reference [5]), and at 1258°K ($D = 5.6 \times 10^{-3} \text{ cm}^2/\text{sec}$., [Reference (5)]), with $r = 75 \times 10^{-4} \text{ cm}$ (upper particle size limit for the precomposed powder) and $22 \times 10^{-4} \text{ cm}$ (lower size limit), and for $t = 10^{-2}$, 10^{-3} , and 10^{-4} seconds. The results are shown in Table 3.

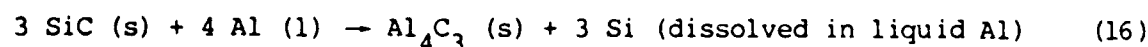
It can be seen that even at 933°K the fractional removal of hydrogen from the

smaller droplets is complete at $t = 10^{-2}$ seconds and approximately 90% complete at $t = 10^{-3}$ seconds. For the larger droplets, 10^{-2} seconds is required for removing 84% of the hydrogen at 933°K . At 1258°K , complete removal of the hydrogen can be achieved from the larger droplets in 10^{-2} seconds and from the smaller droplets in 10^{-3} second. To remove all the hydrogen from the larger droplets at $t = 10^{-3}$ seconds or less, the droplets have to be heated to temperatures higher than 1258°K .

6. Reaction Between the Liquid Al Matrix and the SiC Dispersion.

(1). Reaction between liquid Al and SiC to form Al_4C_3 .

The reaction under consideration is:



The equilibrium activity of Si dissolved in liquid Al, a_{Si}^* , for this reaction was calculated from the standard free energy of reaction F° obtained from the literature (Reference (2)) by using the equation

$$\Delta F^{\circ} = - RT \ln a_{\text{Si}}^* = - 13.714 T \log a_{\text{Si}}^* \quad (17)$$

over the temperature range $1000 - 2300^{\circ}\text{K}$. The results are shown in Table 4.

a_{Si}^* represents the Si activity at the interface between the liquid Al and the SiC dispersed phase when they are in equilibrium. Reaction (16) will proceed

only if the Si formed at the interface is removed continuously by diffusion into the bulk of the liquid Al matrix, and the $\text{Al}_4\text{C}_3(\text{s})$ formed is not a barrier for Si, Al and C transport.

Assume a composite model consisting of alternate layers of SiC and liquid Al of 10^{-3} cm thickness each, with the Si activity at the interface equal to a_{Si}^* . The average Si activity, \bar{a}_{Si} , in the liquid Al layer after a diffusion time of t seconds can be represented by the equation (Reference (4)):

$$R = \frac{\bar{a}_{\text{Si}}}{a_{\text{Si}}^*} = 1 - \frac{8}{\pi^2} \sum_{n=0}^{\infty} \frac{1}{(2n+1)^2} \exp \left[- \left(\frac{(2n+1)\pi}{10^{-3}} \right)^2 Dt \right] \quad (18)$$

where R is defined as the degree of saturation, since when $R = 1$, i.e. $\bar{a}_{\text{Si}} = a_{\text{Si}}^*$, the reaction will stop, and D = diffusion constant for Si in liquid Al. Equation (18) shows that R is a function of Dt . R values for $Dt = 10^{-6}, 10^{-7}, 10^{-8}$, and 10^{-9} cm^2 were calculated using Equation (18). These Dt values were selected because the D values for diffusion in liquid metal systems are usually in the range of 10^{-5} to $10^{-4} \text{ cm}^2/\text{sec}$ (Reference (3)), and the residence time for the composite powder in the plasma is expected to be in the range of 10^{-4} to 10^{-2} second. The calculated R values are given in Table 5.

The depletion of the SiC dispersed phase inventory by Reaction (16) can be calculated as follows. The total number of Si atoms present in the liquid Al layer of 10^{-3} cm thickness and 1 cm^2 cross sectional area, n_{Si} , is related to the average mole fraction \bar{N}_{Si} of Si in this liquid Al layer by the equation:

$$\bar{N}_{Si} = \frac{n_{Si}}{n_{Si} + n_{Al}} \quad (19)$$

where n_{Al} = number of Al atoms in the liquid Al layer (approximately 6.1×10^{19}).

If the solution of Si in Al can be considered as an ideal solution, then $\bar{N}_{Si} = \bar{a}_{Si}$ and from Equation (19)

$$n_{Si} = \frac{\bar{a}_{Si}^*}{1 - \bar{a}_{Si}} \times 6.1 \times 10^{19} = \frac{R a_{Si}^*}{1 - R a_{Si}^*} \times 6.1 \times 10^{19} \quad (20)$$

The total number of Si atoms in the SiC layer of 10^{-3} cm thickness and 1 cm^2 cross sectional area is approximately 4.88×10^{19} .

From Equation (20), the fractional depletion F for the SiC inventory is:

$$F = \frac{n_{Si}}{4.88 \times 10^{19}} = 1.25 \frac{R a_{Si}^*}{1 - R a_{Si}^*} \quad (21)$$

Equation (21) can be used to calculate the loss of the SiC dispersed phase due to reaction with the liquid Al matrix to form Al_4C_3 during plasma processing of

the composite powders as a function of temperature and time if the D values for the diffusion of Si in liquid Al at these temperatures are known. Estimates can be made by assuming a D value of 10^{-5} cm²/sec. at 1000°K and an activation energy for diffusion, Q, of 8000 calories/mole. These assumptions may not be unreasonable considering the diffusion data for liquid metal systems reviewed in Reference (6).

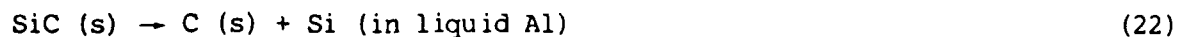
Using $D_{1000^{\circ}\text{K}} = 10^{-5}$ cm²/sec. and $Q = 8000$ calories/mole, the D value for 2300°K was found to be about 10^{-4} cm²/sec. Using these D values, the R and F values for $t = 10^{-2}$, 10^{-3} , and 10^{-4} second were calculated from Equation (18) and Equation (21), respectively. The results are shown in Table 6.

It is interesting to note that the depletion of SiC is less at 2300°K than at 1000°K for $t = 10^{-2}$ second. This is due to the fact that the liquid Al becomes saturated with Si before $t = 10^{-2}$ seconds is reached and that the Si activity at saturation is lower at 2300°K than at 1000°K (0.104 versus 0.226), since Al_4C_3 is less stable at higher temperatures. It is also interesting to see that the F values for the same t values are relatively insensitive to temperature. The loss of SiC can be held to about a few percent if t is approximately 10^{-4} second, about several percent if t is approximately 10^{-3} second, and about twenty percent if t is approximately 10^{-2} second, for both $T = 1000^{\circ}\text{K}$ and $T = 2300^{\circ}\text{K}$.

(6). Other possible reactions.

Since Al_4C_3 is unstable at high temperatures, as indicated by the decrease of the a_{Si}^* value with the increasing temperature (see Table 4), the following

reaction which does not involve the formation of Al_4C_3 , was considered.



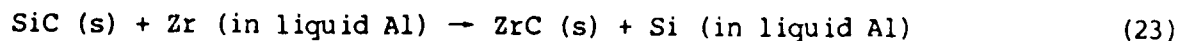
For this reaction, $\Delta F^0 = -RT \ln a_{\text{Si}}^*$. The a_{Si}^* values for 1000, 1500, 2000, and 2300°K were calculated by using thermodynamic data from the literature (Reference (2)). The results are shown in Table 7.

These a_{Si}^* values are much smaller than that for Reaction (16) at the same temperature (see Table 4), suggesting that Reaction (16), not Reaction (22), is favored for the temperature range shown in Tables 3 and 7.

7. Reaction Between the Alloying Elements and the SiC Dispersion.

(1) Reaction between Zr dissolved in liquid Al and SiC.

The reaction under consideration is:



The equilibrium activities of Zr and Si in liquid Al, a_{Zr}^* and a_{Si}^* , are related to the standard free energy of the reaction, ΔF^0 , by the equation.

$$\Delta F^0 = -RT \ln \frac{a_{\text{Si}}^*}{a_{\text{Zr}}^*} = -4.571 T \log \frac{a_{\text{Si}}^*}{a_{\text{Zr}}^*} \quad (24)$$

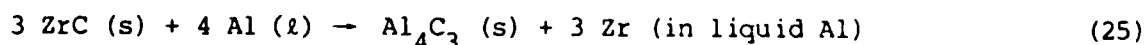
Using thermodynamic data available in the literature (Reference (2)), the values of $a_{\text{Si}}^*/a_{\text{Zr}}^*$ were calculated for the temperature range 1000-2300°K. These calculated values are shown in Table 8. Included in the same table are the a_{Zr}^* values in equilibrium with the a_{Si}^* values given in Table 4 for each of the temperatures indicated in these tables. These are the a_{Zr}^* values needed to maintain the equilibrium a_{Si}^* values high enough to stop Reaction (16). The results in Table 8 show that the $a_{\text{Si}}^*/a_{\text{Zr}}^*$ values are extremely high, implying that Reaction (23) is highly favored. They also show that the a_{Zr}^* values needed to stop Reaction (16) are much lower than that corresponding to the lowest concentration of Zr (0.5 wt. %) in the Al alloy matrix to be used in this program. If the solution of Zr in liquid Al can be considered as ideal, the a_{Zr} for the 0.5 wt. % alloy is 1.49×10^{-3} .

The above analysis shows that it is possible to use Zr additions to the liquid Al matrix to prevent liquid Al from reacting with SiC to form Al_4C_3 since Zr reacts preferentially with SiC rather than Al. The Si formed according to Equation (23), if its activity in the liquid Al is increased to a value higher than the equilibrium Si activity for Reaction (16), can prevent Reaction (16) from happening. However, for the Zr-Al alloy matrix materials used in this program, the Zr concentration is not high enough to accomplish this goal. Even for the alloy containing 3 wt. % Zr, the highest activity of Si attained after all the Zr has reacted with SiC is only 0.009 which is much lower than the equilibrium Si activity.

Use of Al alloys of higher Zr concentration to overcome this problem may be undesirable, since this involves the loss of a significant amount of SiC in order to increase the activity of Si in the Al to the value needed. In fact, a

better approach would be to prealloy the required amount of Si to the Al matrix. However, the possible effect of large additions of Si to the Al on the mechanical properties of the matrix of the composite would have to be carefully considered.

Addition of a small amount (e.g. 0.5-3 wt. %) of Zr to the Al may prevent the reaction of Al with SiC by another mechanism. As shown by the data in Table 8, the SiC reacts preferentially with the Zr rather than with the Al to form a layer of ZrC over the SiC surface, which may act as a barrier to protect the SiC from being attacked by the Al. ZrC is stable toward Al. This can be shown by considering the reaction:



and calculating the equilibrium activity of Zr in liquid Al, a_{Zr}^* , using the standard free energy of the reaction, ΔF^0 , according to the equation:

$$\Delta F^0 = - RT \ln (a_{\text{Zr}}^*)^3 = - 13.714 T \log a_{\text{Zr}}^* \quad (26)$$

The calculated a_{Zr}^* values for 1000-2300°K are given in Table 9. It can be seen that these a_{Zr}^* values are very small, implying that Reaction (25) is not favored and ZrC is very stable toward Al(l) at the temperatures indicated in Table 9.

The thickness of the ZrC layer required for it to be protective must be determined experimentally. The maximum thickness of the ZrC layer which can be formed from the Zr in the two Zr-Al alloys (0.5 and 3 wt. % Zr) used initially

as matrix materials in this program can be calculated by considering a model composite consisting of alternate layers of SiC and liquid Zr-Al alloy of 10^{-3} cm thickness each. For the 0.5 wt. % Zr-Al alloy, the maximum thickness of the ZrC layer which can be formed on the SiC surface on each side of the liquid Zr-Al alloy layer is 1.14×10^{-6} cm. For the 3 wt. % Zr-Al alloy, this thickness is 6.84×10^{-6} cm.

The actual thickness of ZrC formed on the SiC surface during plasma processing can be calculated on the basis of the model composite described above assuming that the rate-determining factor for the growth of the ZrC layer is the transport of Zr from the bulk of the liquid alloy layer to the SiC surface and that the activity of Zr is zero at the SiC surface. The average activity of Zr in the liquid alloy layer, \bar{a}_{Zr} , is related to the residence time in the plasma, t , by the equation (Reference (4)):

$$\frac{\bar{a}_{Zr}}{a_{Zr}^0} = \frac{8}{\pi^2} \sum_{n=0}^{\infty} \frac{1}{(2n+1)^2} \exp \left[- \left(\frac{(2n+1) \pi}{10^{-3}} \right)^2 Dt \right] \quad (27)$$

where D = diffusion constant for Zr in liquid Al at the plasma temperature,

a_{Zr}^0 = initial activity of Zr in the liquid alloy layer,

= 9.09×10^{-3} for the alloy containing 3.0 wt. % Zr,

and 1.49×10^{-3} for the alloy containing 0.5 wt. % Zr.

The fractional depletion of the Zr inventory in the liquid alloy layer, F_d , after time t in the plasma is:

$$F_d = \frac{a_{Zr}^o - \bar{a}_{Zr}}{a_{Zr}^o} = 1 - \frac{8}{\pi^2} \sum_{n=0}^{\infty} \frac{1}{(2n+1)^2} \exp \left[- \left(\frac{(2n+1)\pi}{10^{-3}} \right)^2 Dt \right] \quad (28)$$

The F_d and \bar{a}_{Zr} values for $Dt = 10^{-6}, 10^{-7}, 10^{-8}$ and 10^{-9} cm^2 were calculated, using Equation (28), for the two alloys (0.5 wt. % and 3.0 wt. % Zr) used initially in this program. The results are shown in Table 10.

Included in Table 10 are also the losses of Zr atoms, Δn_{Zr} , from the liquid alloy layer (10^{-3} cm thick, 1 cm^2 cross sectional area) by diffusion to the SiC surface to form ZrC. Δn_{Zr} was calculated from the equation:

$$\Delta n_{Zr} = n_{Zr}^o - n_{Zr} = n_{Zr}^o - \frac{\bar{a}_{Zr}}{1 - \bar{a}_{Zr}} \times n_{Al} \quad (29)$$

where n_{Zr}^o = number of Zr atoms in the liquid alloy layer of 10^{-3} cm thickness and 1 cm^2 cross sectional area

$$= \frac{10^{-3} \text{ cm} \times 1 \text{ cm}^2 \times 2.7 \text{ gm/c.c.} \times (\text{wt. \% Zr})}{91.22 \text{ gm/mole} \times 100} \times 6.1 \times 10^{23}$$

$$= 9.028 \times 10^{16} \text{ for } 0.5 \text{ wt. \% Zr alloy and}$$

$$5.417 \times 10^{17} \text{ for } 3.0 \text{ wt. \% Zr alloy}$$

n_{Zr} = number of Zr atoms in the same liquid alloy layer
after loss by diffusion

$$= \frac{\bar{a}_{Zr}}{1 - \bar{a}_{Zr}} \cdot n_{Al} \text{ if the solution of Zr in Al is ideal}$$

$$\begin{aligned}
 n_{Al} &= \text{number of Al atoms in the same liquid alloy layer} \\
 &= \frac{10^{-3} \text{ cm} \times 1 \text{ cm}^2 \times 2.7 \text{ gm/c.c. (wt. \% Al)}}{27 \text{ gm/mole} \times 100} \times 6.1 \times 10^{23} \\
 &= 6.070 \times 10^{19} \text{ for 0.5 wt. \% alloy and} \\
 &\quad 5.917 \times 10^{19} \text{ for 3.0 wt. \% alloy}
 \end{aligned}$$

The thickness of ZrC formed on the SiC surface can be calculated from Δn_{Zr} as a function of time in the plasma if the D values for the diffusion of Zr in liquid Al at the plasma temperature are known. Assuming $D = 10^{-5} \text{ cm}^2/\text{sec.}$ at 1000°K and $10^{-4} \text{ cm}^2/\text{sec.}$ at 2300°K , the thickness of ZrC formed on the SiC surface at these temperatures for $t = 10^{-2}$, 10^{-3} , and 10^{-4} second was calculated for the two Zr-Al alloys (0.5 wt. % and 3.0 wt. % Zr) used in this program, using 6.73 gm/c.c. as the density of ZrC. The results are shown in Table 11.

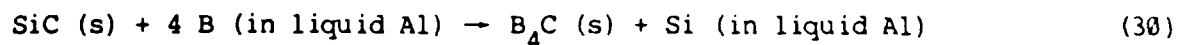
It can be seen that the thickness of ZrC formed on the SiC surface is very thin. Whether such thin ZrC layers can protect SiC from reaction with Al during plasma processing must be determined experimentally.

(2) Reaction between Ti dissolved in Liquid Al and SiC.

The results for Ti-Al alloy matrix are expected to be similar to that for Zr-Al alloy matrix. No analytical calculations were performed.

(3) Reaction between B dissolved in Liquid Al and SiC.

The reaction to be considered is:

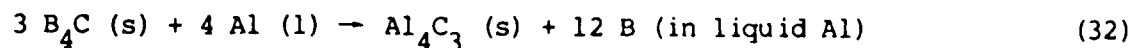


The ratio of the equilibrium activities of B and Si in liquid Al, a_B^* and a_{Si}^* , can be calculated from the standard free energy of reaction, ΔF° , obtained from thermodynamic data in Reference (2), by the equation:

$$\Delta F^\circ = -RT \ln \left(\frac{a_{\text{Si}}^*}{a_B^{*4}} \right) = -4.517 T \log \left(\frac{a_{\text{Si}}^*}{a_B^{*4}} \right) \quad (31)$$

The calculated results for the temperature range 1000 - 2300°K are shown in Table 12. The small values of a_{Si}^*/a_B^{*4} indicate that Reaction (30) is not favored.

Further thermodynamic analysis of the reaction:



shows that any B_4C formed is not stable in liquid Al. The equilibrium activities of B, a_B^* , for the temperature range 1000 - 2300°K, were calculated from the standard free energy of reaction, ΔF° , according to the equation:

$$\Delta F^\circ = -RT \ln a_B^{*12} = -54.85 T \log a_B^* \quad (33)$$

The calculated results are shown in Table 13. The a^* values obtained are larger than or comparable with the a_{Si}^* values for the SiC-Al reaction at the same temperature (see Table 4). This indicates that B_4C is not stable in

liquid. Al at the temperatures indicated in Table 13. The addition of B to the Al matrix therefore cannot prevent the reaction between SiC and Al during plasma processing.

8. Summary of Analytical Results

Analytical results for the major physical and chemical events occurring in the plasma can be summarized as follows:

1. Loss of Al matrix material by evaporation is less than 10% even at 2300°K if the residence time in plasma is less than 10^{-3} second.
2. Losses of (1) Zr, Ti and B alloying elements, (2) SiC, ZrC, and TiC dispersion, and (3) Al_2O_3 film on Al matrix, are negligible at 2300°K for in-plasma residence times as long as 10^{-2} second.
3. Significant amounts of hydrogen dissolved in the Al matrix are lost at the melting point of Al if the residence time in plasma is longer than 10^{-3} second and the presence of an oxide film on the surface of the molten droplets does not impede the removal of hydrogen from droplet surface.
4. SiC will react with the Al matrix to form Al_4C_3 . Loss of SiC by such reaction is about 10% at 2300°K for in-plasma residence time of 10^{-3} second, if the rate limiting factor is the diffusion of the Si produced into the molten Al.
5. Zr and Ti alloying additions will react with SiC to form ZrC and TiC, which

are stable toward Al. For the highest Zr and Ti alloy concentrations used in this program (3 wt. % Zr and 5 wt. % Ti), the maximum thickness of ZrC and TiC formed in a model composite, containing alternate layers of SiC and Al of 10 microns thickness each, are 0.07 micron and 0.17 micron respectively.

6. B alloying additions do not prevent the reaction between SiC and Al. B_4C is not as stable toward Al as ZrC and TiC.

These predictions were compared with the results obtained on the compositions and microstructures of the Al-SiC, Al(Zr)-SiC, Al(Ti)-SiC and Al(B)-SiC feed materials and that of the plasma deposits on inert water-cooled copper substrates at various power levels and distances between the nozzle and the substrate as a prelude to plasma joining of metal matrix composites.

2.0 COMPOSITE POWDER PREPARATION AND EVALUATION

Initial precomposited powders were prepared from 1100 aluminum (commercial purity) and aluminum - 3.0 wt.% Zr powders with a dispersed SiC particulate reinforcing phase. Each composite powder composition contained 25 wt.% of the SiC reinforcing phase.

Figure 1a. shows an optical micrograph at 500 X magnification of the microstructure of cross sections of 1100/SiC precomposited powder particles. The uniformity of dispersion of the reinforcing phase throughout the volume of the composite powder particle is apparent. Figure 1b. shows a scanning electron micrograph of a composite particle cross section at 500 X where the SiC dispersion is more easily seen. Figures 2a. and 2b. show analogous cross

sectional micrographs of precomposited powders prepared with aluminum - 3.0 wt.% Zr alloy matrix and the SiC particulate reinforcing phase.

Additional precomposited powders were prepared with inert gas atomized 1100 aluminum, aluminum - 3.0 wt.% Zr and aluminum - 5.0 wt.% Ti matrix alloys using longer powder processing times. The reinforcing phase used for each precomposited powder type was 30 wt.% (as-received Arco) SiC particulate ranging in size from submicron to approximately 25 microns. Figures 3.-5. show optical micrographs of the as-produced precomposited powders. The composite powder particles are shown in cross-section wherein the dispersion of the SiC particulate phase throughout the microstructure of each powder particle can be clearly seen.

Two composite powder filler metal compositions were prepared in moderate (ca. 1 kg) quantities for use in preparation of larger scale butt welds in Al/SiC composite base plates. The compositions (in wt.%) prepared were Al-8Zr-30 SiC and Al-8Ti-30SiC. Powders were prepared by high energy dry milling of mixtures of aluminum, Al_3Zr , TiAl and SiC particulates, respectively, in inert environments. The powders were milled to macroscopic homogenization as shown in Figures 6 and 7. Final homogenization of the matrix composition was expected to occur during plasma deposition.

Each of these latter compositions was designed to provide higher reactive metal concentrations than have used previously while maintaining a two-phase (Al(Zr) - Al_3Zr and Al(Ti) - Al_3Ti , respectively) matrix microstructure. This represents an attempt to maintain a reasonably ductile matrix phase while providing higher reactive metal concentrations for suppression of interfacial

Al_4C_3 formation during plasma processing. The Al-Zr and Al-Ti phase diagrams are shown in Figure 8. Note the Al-11.4 wt.% Zr and Al-11.4 wt.% Ti matrix phase compositions lie in two-phase regions.

3.0 LOW-PRESSURE PLASMA DEPOSITION

The as-received inert gas atomized matrix alloy powders and precomposited powders were used for initial low-pressure plasma deposition experiments on inert substrates. The inert substrates were thin stainless steel coupons mounted on a water-cooled copper chill to maintain the substrate at a low temperature during deposition. Plasma deposits of various thicknesses were prepared from each alloy and composite powder type with one exception. The Al-3.0 wt.% Zr atomized alloy powder was inadvertently excluded from the first deposition trials and was included in later tests. For the precomposited powders, oversprayed powder, i. e. that which missed the substrate and solidified in flight in the vacuum chamber, was collected for comparison to the starting powders and to the deposited material. Low-pressure plasma deposition process parameters used are shown in Table 14.

The initial series of deposits was produced without a transferred arc between the plasma torch and the substrate or deposit surface. Both the plasma deposited coatings and the overspray powders were mounted in a conductive medium and polished for optical microscopy, scanning electron microscopy and electron beam microprobe examination for microchemical analysis. The polished deposits and overspray powder were examined and photographed in the unetched condition as were the as-produced composite powders shown previously.

Figure 9. shows the microstructure of the low pressure plasma deposited 1100 alloy while Figure 10. shows the analogous 1100 aluminum - 30 wt.% SiC composite deposit. The oversprayed 1100 aluminum - 30 wt.% SiC composite powder is shown in Figure 11. In Figure 9., a few isolated SiC particulates can be seen in the microstructure, the result of trace contamination of the powder feed system. Comparison of Figures 9. and 10. shows the uniform dispersion of SiC in the composite deposit (Figure 10.) as desired. In each micrograph the interface at the bottom of the micrograph is the bond line between the coating and the stainless steel substrate panel. Thus the objective of producing high quality, dense, well-bonded, uniformly reinforced composite deposits or coatings by low pressure plasma deposition of precomposited powders was achieved.

The oversprayed 1100 aluminum - 30 wt.% SiC composite powders are shown in Figure 11. Comparing these to the as-produced powders of this type (Figure 3.) shows that considerable fragmentation of the precomposited powder occurs during plasma processing and that the dispersion of reinforcing phase in the fragments is non-uniform.

Figure 12 shows the microstructure of the aluminum - 3.0 wt.% Zr - 30 wt.% SiC composite deposit wherein the dispersion of the SiC particulate phase can be clearly seen. Comparing this figure to Figure 10. shows that the aluminum - Zr alloy matrix composite deposit is somewhat less dense and less uniformly reinforced than the 1100 aluminum alloy matrix deposit. Comparing the overspray powder of the aluminum - Zr alloy matrix composite, Figure 13., to the as-produced precomposited powders of this type (Figure 4.) shows the same fragmentation during plasma processing and non-uniform reinforcement of the

fragments noted above for the 1100 aluminum alloy matrix composite powders.

Figure 14 shows the microstructure of the aluminum - 5.0 wt.% Ti alloy low pressure plasma deposit. A significant amount of second phase, presumably Al_3Ti , is present in the microstructure as would be expected. The aluminum - 5.0 wt.% Ti - 30 wt.% SiC composite powder particles adhered to the stainless steel substrate only in a few areas after deposition, the reason for which is unknown at present. One such area is shown in Figure 15. There appears to be a reaction layer present at the surface of the stainless steel substrate. Where the deposit adhered, it was uniformly reinforced with SiC, but quite porous compared to the other two composite deposits (Figures 10 and 12). Overspray powder of the aluminum - 5.0 wt.% Ti - 30 wt.% SiC composite powder is shown in Figure 16. Comparing this figure to Figure 5. shows that the uniform SiC dispersion of the starting material is retained but that no fragmentation of the composite powder occurred during plasma processing. Taken together, the evidence suggests that the aluminum - 5.0 wt.% Ti - 30 wt.% SiC composite powder simply did not reach a sufficient temperature during plasma processing to produce a dense, strongly adherent composite deposit.

Microchemical characterization was performed on two types of low-pressure plasma processed precomposited powders which were allowed to solidify in free flight and thus did not impinge upon the water-cooled substrate, i. e. were overspray material not incorporated into a deposit, and compare the results to the starting precomposited powders.

Figure 17 shows the C and Si microprobe traces across a representative large SiC particle in the microstructure of the as-produced 1100 - 30 wt.% SiC_p

precomposited powder. The SiC particle showed edge X-ray resolution of 2 microns which is approximately equal to the theoretical resolution at the 15 KV beam voltage used. Corrected X-ray intensity ratios for Si and C are 30:1 for the as-produced material which is assumed to contain stoichiometric silicon carbide. For comparison, Figure 18 shows the microprobe traces obtained for low pressure plasma-processed 1100 - 30 wt.% SiC_p precomposited powders. The most striking feature of the microstructure of the plasma-processed powder is the significant reduction in the number of large SiC particles present in the microstructure. A backscattered electron image showing the microprobe trace is shown in Figure 19. The majority of SiC particles in the microstructure were found to be less than 5 microns in diameter which is nearly a factor of three smaller than in the as-produced powders. As shown in Figure 19, the microprobe trace passes through two of the small SiC particulates. The peak X-ray intensities for Si and C are reduced to a ratio of 20.4 suggesting possible loss of Si due to vaporization, however the small SiC particle size may affect this result since the SiC particle size now is only twice the theoretical resolution limit. The resolution does not permit inference as to possible increases in C concentration at the particle/matrix interface caused by plasma processing (compare C profiles in Figure 18 to those in Figure 17. Such increases in C concentration might suggest the presence of Al₄C₃ at the particle/matrix interface. The shape of the Si profile near the interface does suggest possible Si dissolution into the matrix as would be expected if Al₄C₃ is formed at the interface, however.

Figure 20 shows the microprobe traces for the as-produced aluminum - 5 wt.% titanium - 30 wt.% SiC_p powders. Figure 21 shows a backscattered electron image of the microstructure corresponding to the microprobe trace in Figure 20.

The microprobe trace shown in Figure 20 indicates a loss of edge resolution for the SiC particulates (to about 4 microns) suggesting that some Ti/SiC reaction may have occurred during low-temperature processing, although this seems highly unlikely. The Si:C peak X-ray intensity ratio is only 13.5 and the C and Si peak intensities are slightly displaced. Both of these observations are believed to be artifacts of the measurement techniques used. The titanium concentration curves indicate the presence of fine Ti-rich phase particles in the matrix phase as noted previously in metallographic examination. Figure 22 shows the microprobe traces for the low-pressure plasma processed aluminum - 5 wt.% titanium - 30 wt.% SiC_p powders. The corresponding backscattered electron micrograph is shown in Figure 23. As above, a reduction in average SiC particle size is noted after plasma processing. The SiC peak X-ray intensity ratio is now measured at 24.4 which is in reasonable agreement with the measurements on the plasma processed 1100 - 30 wt.% SiC_p powders. The titanium concentration shows an apparent buildup in the near-interfacial matrix phase suggesting some interfacial TiC formation and does not show the "peaking" in one matrix away from the interface which would be expected if Ti-rich intermetallics were present. A high Ti concentration may possibly have been "quenched in" to form a non-equilibrium microstructure devoid of the Al₃Ti phase. No clear evidence of the expected interfacial TiC formation is found, but again the resolution is too low to observe this interfacial phase directly.

The microchemical differences observed between as-produced precomposited powders and those which had been plasma processed and allowed to solidify in free flight were just described. This section describes microstructural and microchemical characterization of low pressure, transferred arc plasma deposits produced on inert substrates. The plasma deposited composite powders described

herein impinged on an inert, stainless steel substrate backed by a water-cooled copper chill block to prevent substrate softening and melting. Three types of precomposited powders were used as feed material in these experiments. These were the previously used 1100 aluminum - 30 wt.% SiC_p and aluminum - 5 wt.% Ti - 30 wt.% SiC_p and also aluminum - 3 wt.% Zr - 30 wt.% SiC_p.

Figure 24 shows the C and Si microprobe traces across a representative SiC particle in the microstructure of the 1100 aluminum - 30 wt.% SiC_p deposit. The SiC particle showed edge X-ray resolution of 4 microns which was slightly lower than reported previously for the as-produced powder. Corrected X-ray intensity ratios for Si and C are 31:1 which is virtually identical to the starting powder. The average SiC particle size is similar to that of the starting powder unlike that observed in the composite powder allowed to solidify in free flight where substantial fragmentation of the SiC phase within the composite powder particles was observed. It was concluded that microchemical differences between the starting powders and the dense, solid deposits are minimal for this baseline system.

Figure 25 shows C, Si, and Ti microprobe traces near and across a representative SiC particle in the microstructure of the dense aluminum - 5 wt.% Ti - 30 wt.% SiC_p deposit. The SiC X-ray intensity ratio was 25 in reasonable agreement with the starting powders. The average SiC phase particle size was reduced with respect to the starting powders as previously observed for composite powders allowed to solidify in free flight. Figure 26 shows a second microprobe trace through the same SiC particle. The SiC ratio was 29.6 in good agreement with the starting powders. For both microprobe traces, Ti-rich phase particles were observed in the matrix alloys unlike the case of the powders

allowed to solidify in free flight where excess titanium was apparently "quenched-in" to the matrix alloy. The slower cooling rate of the solid deposit likely results in Al_3Ti precipitation and growth in the matrix alloy. The most striking feature of the microprobe traces shown in Figures 25 and 26 is the appearance of an apparent Ti-rich reaction zone at the particle/matrix interface as might be expected under relatively slow cooling conditions. The interfacial phase, probably TiC_{1-x} , is both expected and desired to suppress Al_4C_3 formation at the interface. A backscattered electron image of the SiC particle and the paths of the two microprobe traces shown in Figures 25 and 26 is shown in Figure 27. The white second phase visible in the matrix is the Ti-rich phase.

Figures 28 and 29 show the C, Si and Zr microprobe traces across a representative SiC particle in the microstructure of the aluminum - 3 wt.% Zr - 30 wt.% SiC_p deposit and the corresponding backscattered electron image of the SiC particle and trace path, respectively. Similarly, Figures 30 and 31 show C, Si, and Zr microprobe traces across a different SiC particle in the same microstructure and the trace path, respectively. (Figures 28 and 29 are at a magnification of 4000X, Figures 30 and 31 at 2000X). The average size of the SiC phase particles was compared to the starting powders above for the Ti-containing matrix alloy. The SiC X-ray intensity ratios were 33 and 32 for these two particles which values are similar to the starting materials. A Zr-rich phase, likely Al_3Zr , is observed in the matrix microstructure as in the starting powders. No Zr-rich region was detected at the particle/matrix interface unlike the case for the Ti-containing matrix composition. The thickness of this region is predicted to be substantially below the resolution limit of the microprobe for the short plasma residence times employed in this

study, however, and even after relatively slow cooling in the deposits may still be below the resolution limit.

Thus low pressure, transferred arc plasma processing onto inert substrates had no detrimental effect on either the baseline or reactive metal-containing matrix alloy composite compositions. (The reduction in SiC particle size in the plasma deposited material is not considered detrimental). The possible formation of protective, reactive metal rich interfacial phases may in fact be quite beneficial to the properties of the composite deposits.

The composite powders were also deposited by the low pressure, transferred arc process into a 60° included angle, single bevel joint in 0.25 in. thick 6061 aluminum - 30 wt.% SiC_p composite base plates. Thus these were the first actual welds prepared with composite powder filler metals by the low pressure, transferred arc "welding" process. Plasma processing conditions were similar to those previously described (Table 14) with the imposition of a higher intensity transferred arc between the plasma torch and the 6061-30 SiC_p base metal plates to achieve significant melt-in of the base plate. The plates were mounted on the same water-cooled copper chill block used previously to cool inert stainless steel substrate plates. Thus the difference between procedures used to produce dense deposits on inert substrates and those used to produce butt welds in composite base plates was primarily the use of a more intense transferred arc in the latter case.

Figure 32 shows an optical micrograph (unetched) at 500X of the fusion line observed for the 6061-30 SiC_p base plate welded with 1100 aluminum - 30 wt.% SiC_p composite filler metal. The base plate microstructure is at the lower

left, the composite weld metal microstructure at the upper right, and the fusion line running from upper left to lower right. Several features are noteworthy. The fusion line is exceptionally clean and well bonded although a thin layer is seen to be free of SiC particulates. Microporosity is evident in both the weld metal and base metal heat affected zone microstructures (however in both cases it is no more severe than that observed in the as-received base metal). The weld metal can be seen to be uniformly reinforced with SiC and thus is a true composite weld metal as desired. This represents achievement of a major objective of the current program, the production of true composite microstructures in fusion welds by the plasma welding technique.

Figures 33 and 34 show the weldment structures produced using aluminum - 5 wt.% Ti - 30 wt.% SiC_p and aluminum - 3 wt.% Zr - 30 wt.% SiC_p composite filler metals, respectively. The weld metal, base metal and fusion line orientations are identical to those shown in Figure 32. Both weld metal microstructures are uniformly reinforced composites as desired. In both cases, the fusion line microstructure is clean and reinforced with SiC unlike that shown in Figure 32. The reason for incorporation of SiC in the fusion line microstructure when reactive metals are present in the filler metal matrix alloy composition is not yet known. Both weld metals shown in Figures 33 and 34 have reduced levels of microporosity compared to that observed in Figure 32. In all three photomicrographs, no obvious degradation of the base metal microstructure is observed near the fusion line, i.e. there is no classical, coarse-grained heat affected zone evident.

Electron beam microprobe examinations were made on near-fusion line regions of

the butt welds. Figure 35 shows a backscattered electron image of the near-fusion line microstructures observed for a weld produced using 1100 aluminum - 30 wt.% SiC_p filler metal and also shows the path of the electron beam microprobe trace across the fusion line. The most interesting feature of the micrograph is the band of light colored material along the fusion line. In optical metallographic examination, this band appeared to be free of SiC particulates, however electron metallographic examination revealed that this band actually contains very finely dispersed SiC fragments. These apparently form by disintegration of the large SiC particulates present in the starting filler metal and present intact throughout most of the weld metal microstructure. Isolated islands of matrix phase containing very fine SiC particulates were also found in the weld metal microstructure.

Figure 36 shows a similar micrograph of a weld produced using an aluminum - 3 wt.% Zr - 30 wt.% SiC_p filler metal. The band of light colored material containing finely dispersed SiC along the fusion line is much narrower for this filler metal composition but still present. No islands of matrix phase containing finely divided SiC particulates were found in the weld metal microstructure.

Figure 37 shows a similar micrograph of a weld produced using aluminum - 5 wt.% Ti - 30 wt.% SiC_p filler metal. No band of material containing finely dispersed SiC is present along the fusion line. No islands of matrix phase containing finely divided SiC particulates were found in the weld metal microstructure.

The 1100 aluminum - 30 wt.% SiC_p filler metal composition would be expected to

show the most extensive matrix/reinforcing phase chemical reactions during plasma processing. The tendency for formation of regions containing very finely dispersed SiC particulates at the fusion line and in the bulk of the weld metal may be related to the extent of such reactions during plasma processing. Disintegration of the large SiC particulates present in the starting filler material is obviously less in those filler metal compositions containing reactive metal additions. The reactive metal additions also reduce the likelihood of interfacial Al_4C_3 formation by matrix/reinforcing chemical interactions.

Figure 38 shows electron beam microprobe traces for Si and C across the heat affected zone, fusion line and weld metal on the path shown in Figure 35. The path traverses two large SiC particles, A which is in the weld metal and B which is in the heat affected zone. The "band" refers to the fusion line microstructural zone containing finely divided SiC. The traces do not provide sufficient resolution for positive identification of interfacial reactions however they suggest the possibility of such reactions at the fusion line (in the "band") where the peak Si and C concentrations are not in synchronization as they should be for unreacted SiC.

Figure 39 shows similar microprobe traces for Si, C, and Zr across the heat affected zone, fusion line and weld metal on the path shown in Figure 36. The path traverses large SiC particles A in the weld metal and B in the heat affected zone. No evidence of possible interfacial reactions is noted at or near the fusion line. No evidence for Zr diffusion into the base metal is observed. The Zr concentration spikes in the weld metal are locations of the Al_3Zr second phase present in the matrix alloy.

Figure 40 shows similar microprobe traces for Si, C, and Ti across the heat affected zone, fusion line and weld metal on the path shown in Figure 37. The path traverses large SiC particles A in the weld metal and B, C, and D in the heat affected zone. The fusion line interface is quite sharp with no "particle-free" band present. No evidence for particle/matrix interfacial chemical interaction is resolved in either the weld or heat affected zone. No evidence for Ti diffusion into the base metal is observed.

4.0 MECHANICAL TESTING

Additional butt welds were prepared in 0.25 in. thick material (6061 - 30% SiC_p) using welding procedures similar to those shown in Table 14. The joint design used was a single bevel, 90° included angle, 0.25 in. root opening. Filler metals used were the Al - 8Zr - 30SiC_p and Al - 8Ti - 30SiC_p compositions described previously. The welds were used both for metallographic examination and for transverse tensile testing. Square cross section tensile specimens (1 cm x 1 cm cross section) were wire EDMed from the welded plates to attempt to minimize cracking of the weld area, although some microcracking was observed after EDMing.

Figures 41 and 42 show metallographic cross sections of the fusion line regions. The Al - 8Zr - 30 SiC_p weld shows a rather thick "particle-free" zone at the fusion line while the Al - 8Ti - 30 SiC_p weld shows particulate reinforcement extending up to the fusion line as desired. At this point the most likely cause of the apparent particle-free zone is felt to be disintegration of the reinforcing phase in and the initially deposited

composite weld metal as described previously.

Transverse tensile properties are shown in Table 15. These first results would have to be considered quite encouraging. The specimens, with one exception, fractured in the weld metal along pre-existing porosity. The highest strength specimen fractured near, but not at, the fusion line, therefore the bond line strength is in excess of 17.5 ksi in the as-deposited condition. Subsequent densification such as HIPing, would almost certainly improve these strength levels considerably. Similarly, further optimization of the deposition/welding process to reduce porosity would be expected to produce higher joint efficiencies.

5.0 REFERENCES

1. Appendix VI, by John L. Margrave, in "Physicochemical Measurements at High Temperatures, edited by J. O'M. Bockris, J. L. White, and J. D. Mackenzie, Butterworths Scientific Publications, London, 1959.
2. JANAF Thermochemical Tables, Second Edition, July, 1970.
3. Contributions to the Data on Theoretical Metallurgy, XII, "Heats and Free Energies of Formation of Inorganic Oxides," by James P. Coughlin, Bulletin 542, Bureau of Mines, 1954.
4. Diffusion in Solids, Liquids, and Gases, by W. Jost, p. 46. Academic Press, New York, 1952.
5. A. Vashchenko, et al, Invest. Met., 15, No. 1, pp. 50-56, (1972).
6. L. Yang and G. Derge "General Consideration of Diffusion in Melts of Metallurgical Interest", Proceedings of Metallurgical Society Conferences, Volume 7, Physical Chemistry of Process Metallurgy, Part I, p. 503.

Table 1

Fractional Decrease Of Al Droplet Radius As A Function
Of Temperature And Time Of Residence In Plasma

(A) Droplet Radius = 75×10^{-4}

<u>Temperature (°K)*</u>	<u>Residence Time in Plasma</u>		
	10^{-2} sec.	10^{-3} sec.	10^{-4} sec.
950	4.85×10^{-11}	4.85×10^{-12}	4.85×10^{-13}
1080	4.55×10^{-9}	4.55×10^{-10}	4.55×10^{-11}
1245	4.24×10^{-7}	4.24×10^{-8}	4.24×10^{-9}
1480	3.89×10^{-5}	3.89×10^{-6}	3.89×10^{-7}
1820	3.51×10^{-3}	3.51×10^{-4}	3.51×10^{-5}
2350	3.08×10^{-1}	3.08×10^{-2}	3.08×10^{-3}

(B) Droplet Radius = 22×10^{-4}

<u>Temperature (°K)*</u>	<u>Residence Time in Plasma</u>		
	10^{-2} sec.	10^{-3} sec.	10^{-4} sec.
950	1.65×10^{-10}	1.65×10^{-11}	1.65×10^{-12}
1080	1.55×10^{-8}	1.55×10^{-9}	1.55×10^{-10}
1245	1.45×10^{-6}	1.45×10^{-7}	1.45×10^{-8}
1480	1.33×10^{-4}	1.33×10^{-5}	1.33×10^{-6}
1820	1.20×10^{-2}	1.20×10^{-3}	1.20×10^{-2}
2350	1.05	1.05×10^{-1}	1.05×10^{-2}

* Vapor pressure of Al at these temperatures obtained from Reference (1).

Table 2

Equilibrium Pressures of Al_2O and AlO over Al_2O_3 At Various Temperatures

$T (^{\circ}\text{K})$	$p_{\text{Al}_2\text{O}}(\text{atm.})$	$p_{\text{AlO}}(\text{atm.})$
1000	9.68×10^{-30}	2.41×10^{-27}
1500	1.04×10^{-16}	2.46×10^{-15}
2000	3.41×10^{-10}	2.48×10^{-9}
2300	1.21×10^{-7}	5.55×10^{-7}

Table 3

Removal of Hydrogen From Molten Al Alloy Droplets in Plasma

Radius of Molten Al Alloy Droplets (cm)	Residence Time In Plasma (sec.)	Fractional Removal of Hydrogen From Droplets	
		933°K	1258°K
75 X 10 ⁻⁴	10 ⁻²	0.84	1.00
	10 ⁻³	0.35	0.77
	10 ⁻⁴	0.12	0.31
22 X 10 ⁻⁴	10 ⁻²	1.00	1.00
	10 ⁻³	0.87	1.00
	10 ⁻⁴	0.38	0.81

Table 4

Equilibrium Si Activity, a_{Si}^* , for Reaction (1). at Various Temperatures

Temperature ($^{\circ}\text{K}$)	a_{Si}^*
1000	0.226
1100	0.200
1200	0.180
1300	0.165
1400	0.152
1500	0.142
1600	0.135
1700	0.128
1800	0.122
1900	0.118
2000	0.113
2100	0.110
2200	0.107
2300	0.104

Table 5

Degree of Saturation for Si in Liquid Al for Various Dt Values

Dt (cm ²)	Degree of Saturation (R)
10 ⁻⁶	1
10 ⁻⁷	0.698
10 ⁻⁸	0.229
10 ⁻⁹	0.075

Table 6

Depletion of SiC Dispersed Phase by Reaction with Liquid Al Matrix to Form Al_4C_3

$T(^{\circ}\text{K})$	$D(\text{cm}^2/\text{sec})$	a_{Si}^*	$t(\text{seconds})$	R	F
1000	10^{-5}	0.226	10^{-2}	0.698	0.234
			10^{-3}	0.229	0.068
			10^{-4}	0.075	0.022
2300	10^{-4}	0.104	10^{-2}	1	0.145
			10^{-3}	0.698	0.098
			10^{-4}	0.229	0.030

Table 7

Equilibrium Si Activity for Reaction (7)

$T^{\circ}\text{K}$	a_{Si}^*
1000	3.83×10^{-4}
1500	7.12×10^{-3}
2000	0.031
2300	0.054

Table 8

Thermodynamic Evaluation of Reaction (23)

$T^{\circ}\text{K}$	$a_{\text{Si}}^*/a_{\text{Zr}}^*$	a_{Zr}^* Needed to Prevent Reaction(1
1000	2.31×10^6	9.78×10^{-8}
1100	6.08×10^5	3.28×10^{-7}
1200	1.95×10^5	9.21×10^{-7}
1300	7.37×10^4	2.23×10^{-6}
1400	3.20×10^4	4.75×10^{-6}
1500	1.55×10^4	9.16×10^{-6}
1600	9.11×10^3	1.48×10^{-5}
1700	4.69×10^3	2.73×10^{-5}
1800	2.85×10^3	4.28×10^{-5}
1900	1.82×10^3	6.48×10^{-5}
2000	1.22×10^3	9.26×10^{-5}
2100	8.52×10^2	1.29×10^{-4}
2200	6.12×10^2	1.75×10^{-4}
2300	4.53×10^2	2.30×10^{-4}

Table 9

Thermodynamic Evaluation of the Reaction Between ZrC and Al(l)

$T^{\circ}\text{K}$	a_{Zr}^*
1000	9.77×10^{-8}
1100	3.29×10^{-7}
1200	9.22×10^{-7}
1300	2.23×10^{-6}
1400	4.77×10^{-6}
1500	9.19×10^{-6}
1600	1.65×10^{-5}
1700	2.72×10^{-5}
1800	4.30×10^{-5}
1900	6.48×10^{-5}
2000	9.30×10^{-5}
2100	1.29×10^{-4}
2200	1.75×10^{-4}
2300	2.29×10^{-4}

Table 10

Loss of Zr Atoms from Liquid Zr-Al Alloys by Diffusion to the Surface of SiC to Form ZrC

$Dt(\text{cm}^2) F_d$	a_{Zr}		Δn_{Zr}		
	0.5 wt.% Zr [*]	3.0 wt.% Zr ^{**}	0.5 wt.% Zr	3.0 wt.% Zr	
10^{-6}	1.0	0	0	9.028×10^{16}	5.417×10^{17}
10^{-7}	0.698	4.50×10^{-4}	2.75×10^{-3}	6.297×10^{16}	3.790×10^{17}
10^{-8}	0.229	1.15×10^{-3}	7.01×10^{-3}	2.048×10^{16}	1.269×10^{17}
10^{-9}	0.075	1.38×10^{-3}	8.41×10^{-3}	6.521×10^{15}	4.408×10^{16}

$$^* a_{\text{Zr}}^0 = 1.49 \times 10^{-3}$$

$$^{**} a_{\text{Zr}}^0 = 9.09 \times 10^{-3}$$

Table 11

Thickness of ZrC Formed on SiC Surface at 1000
and 2300°K as a Function of Time in Plasma

T°K	D(cm ² /Sec)	t(seconds)	Thickness of ZrC on SiC (cm)	
			0.5 wt.% Zr Alloy	3.0 wt.% Zr Alloy
1000	10 ⁻⁵	10 ⁻²	7.92 x 10 ⁻⁷	4.76 x 10 ⁻⁶
		10 ⁻³	2.57 x 10 ⁻⁷	1.60 x 10 ⁻⁶
		10 ⁻⁴	8.20 x 10 ⁻⁸	1.11 x 10 ⁻⁶
2300	10 ⁻⁴	10 ⁻²	1.14 x 10 ⁻⁶	6.84 x 10 ⁻⁶
		10 ⁻³	7.92 x 10 ⁻⁷	4.76 x 10 ⁻⁶
		10 ⁻⁴	2.52 x 10 ⁻⁷	1.60 x 10 ⁻⁶

Table 12

Thermodynamic Evaluation of B and SiC in Liquid Al

$T(^{\circ}\text{K})$	$a_{\text{Si}}^*/a_{\text{B}}^{*4}$
1000	0.032
1200	0.060
1400	0.092
1600	0.126
1800	0.160
2000	0.195
2200	0.228
2300	0.245

Table 13

Thermodynamic Analysis of the Reaction Between B_4C and Al

$T(^{\circ}K)$	a_B^*
1000	1.63
1200	1.32
1400	1.13
1600	1.02
1800	0.44
2000	0.20
2200	0.10
2300	0.08

Table 14

Low-Pressure Plasma Deposition Process Parameters

Voltage	47 V.
Amperage	1200 A.
Primary Argon Pressure (#56 Orifice)	250 psig.
Secondary Helium Pressure (#80 Orifice)	100 psig.
Hopper Carrier Gas Pressure (#77 Orifice)	120 psig.
Arc Gas Pressure	70 psig.
Chamber Argon Backfill Pressure	30 torr.
Powder Feed Rate	21 g/min.
Spray Distance	12 in.

Table 15

ROOM TEMPERATURE TENSILE TEST RESULTS

<u>I.D. No.</u>	<u>UTS (ksi)</u>	<u>Fracture Location</u>
Al-8Zr-30SiC		
1	16.7	Weld
2	17.5	Near Fusion Line
6	13.5	Weld
7	13.6	Weld
Al-8Ti-30SiC		
1	13.1	Weld
2	11.2	Weld
5	10.3	Weld
6	10.6	Weld

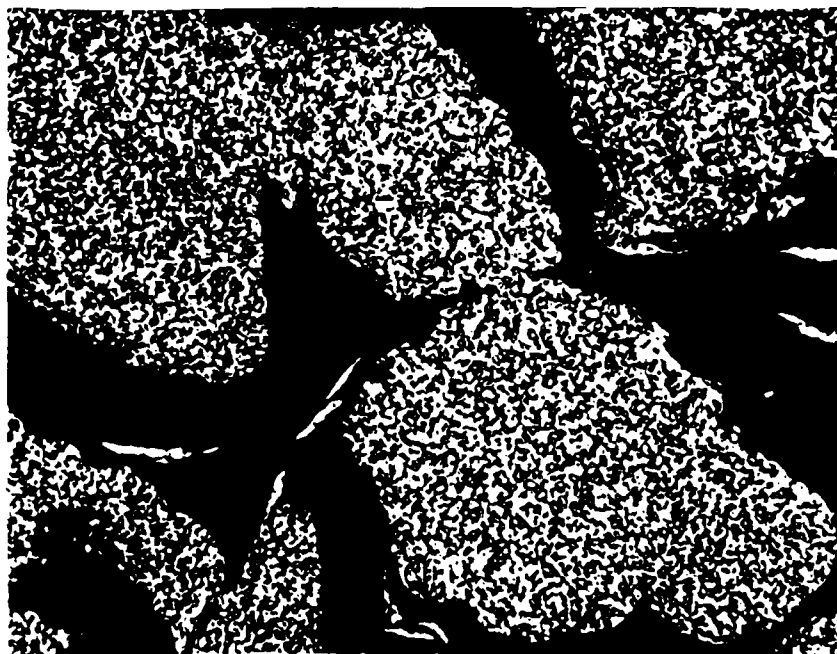


Figure 1a. Cross sections of 1100 aluminum/SiC precomposited powders.
Magnification (500X)



Figure 1b. Cross section of 1100 aluminum/SiC precomposited powder.
Scanning electron micrograph. Magnification (5000X)

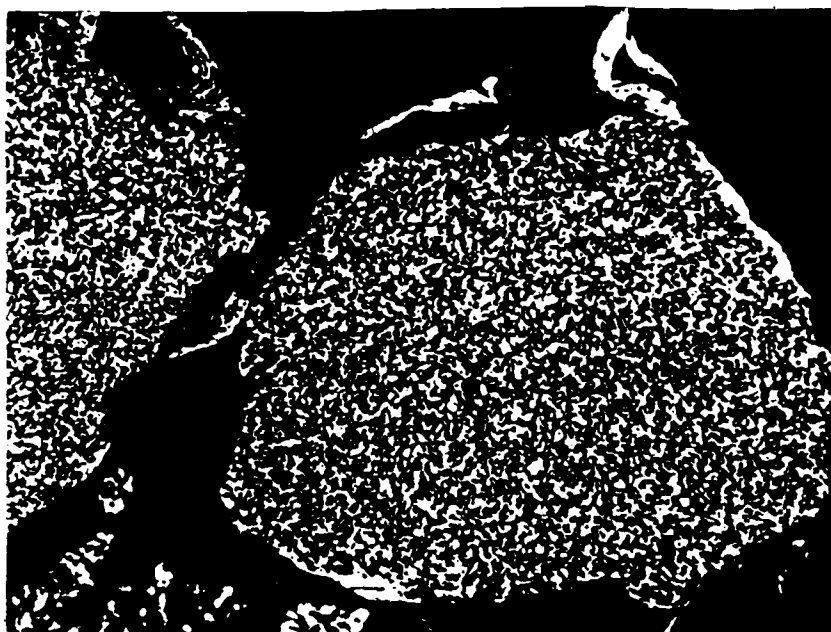


Figure 2a. Cross sections of aluminum - 3.0 wt.% Zr/SiC precomposited powders. Magnification (500X)

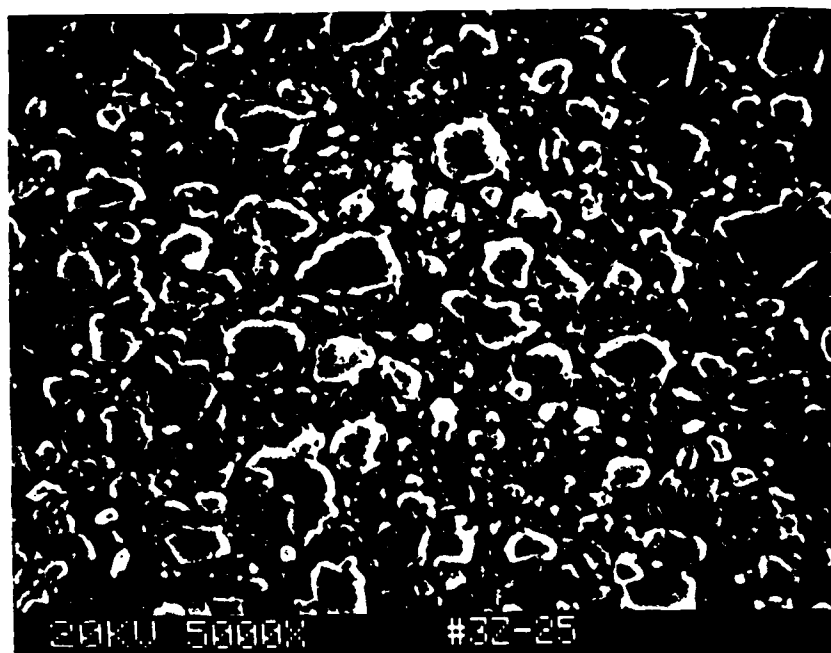


Figure 2b. Cross section of aluminum - 3.0 wt.% Zr/SiC precomposited powder. Scanning electron micrograph. Magnification (5000X)

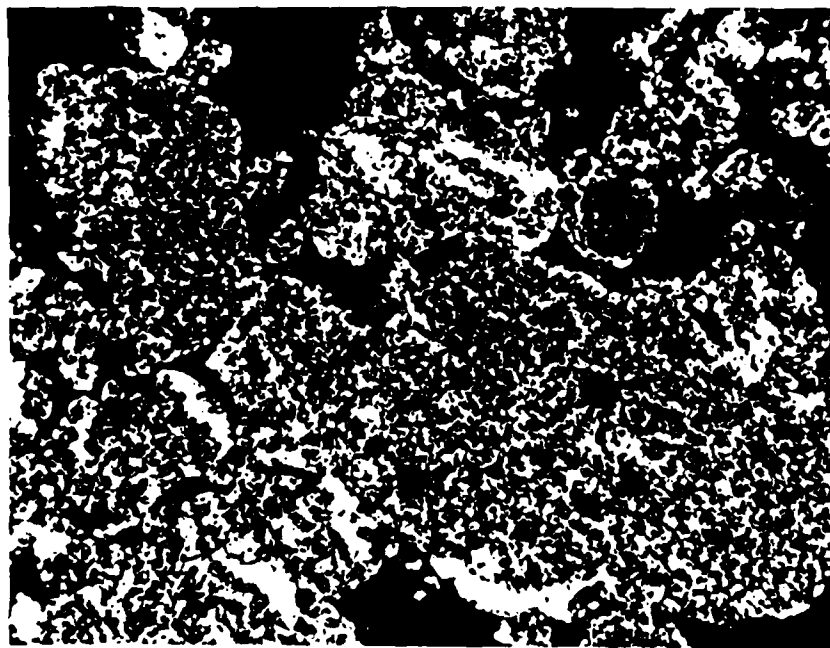


Figure 3. Precomposited 1100 Al - 30 wt.% SiC_p powder particles.
(500X).

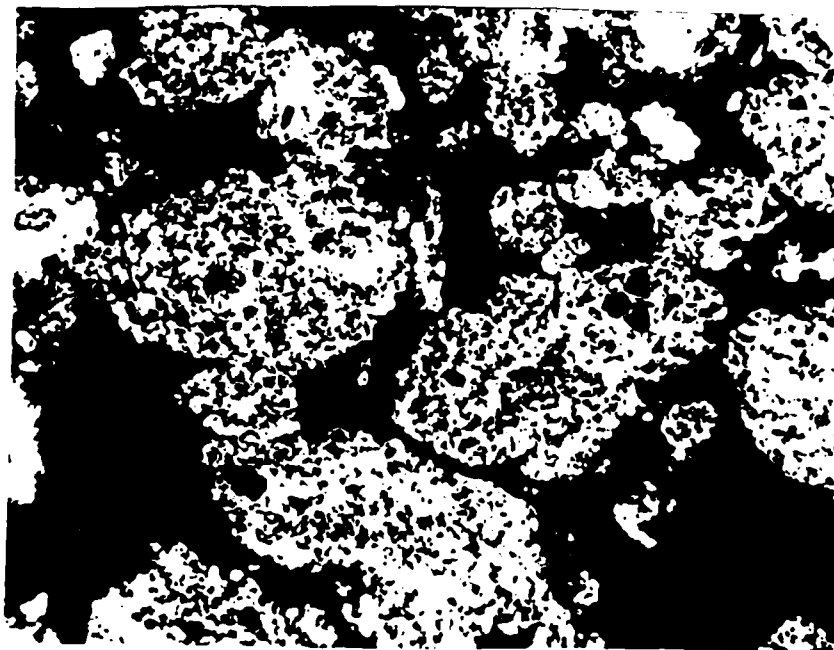


Figure 4. Precomposited Al - 3.0 wt.% Zr - 30 wt.% SiC_p powder particles. (500X).

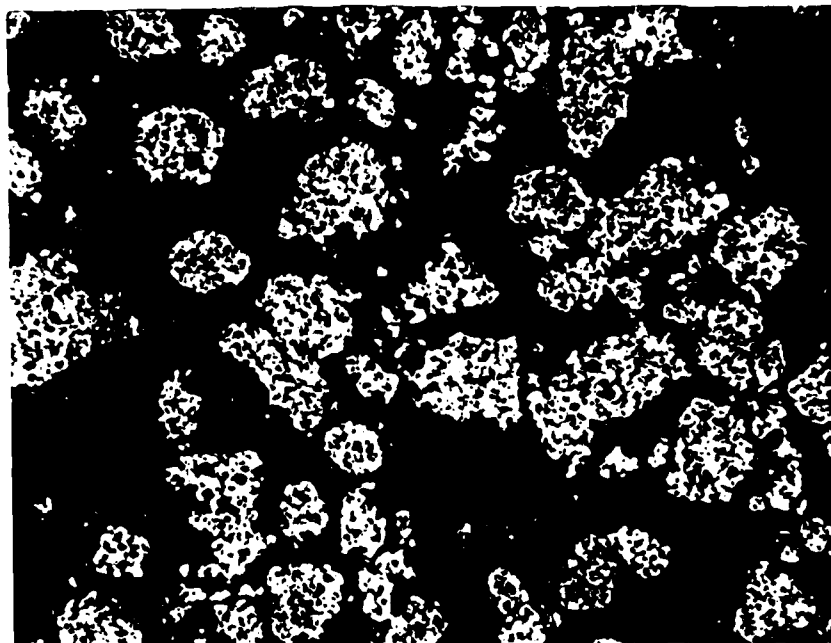


Figure 5. Precomposited Al - 5.0 wt.% Ti - 30 wt.% SiC_p powder particles. (500X).

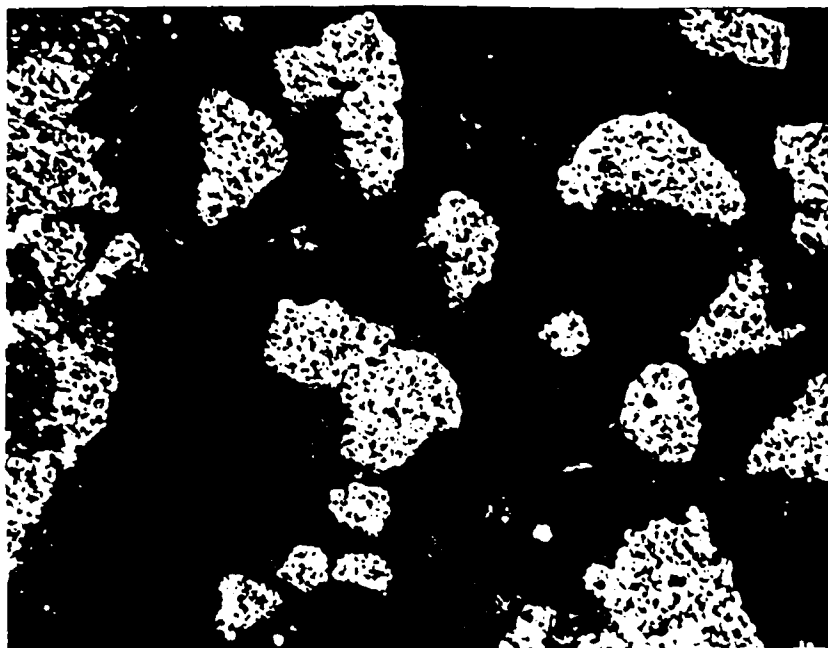
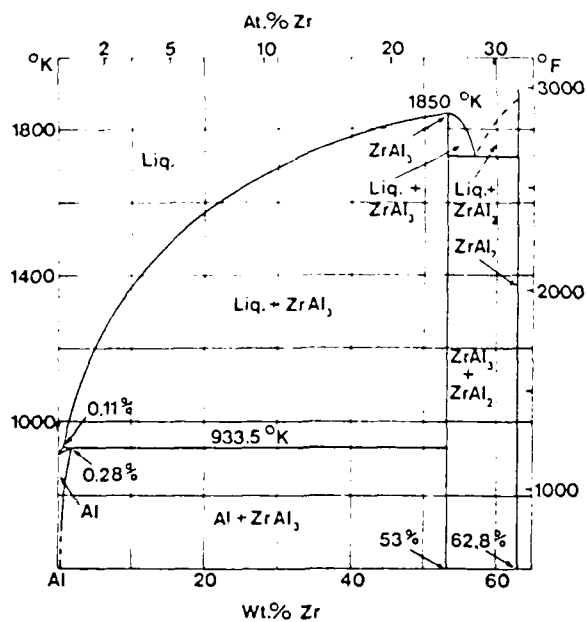


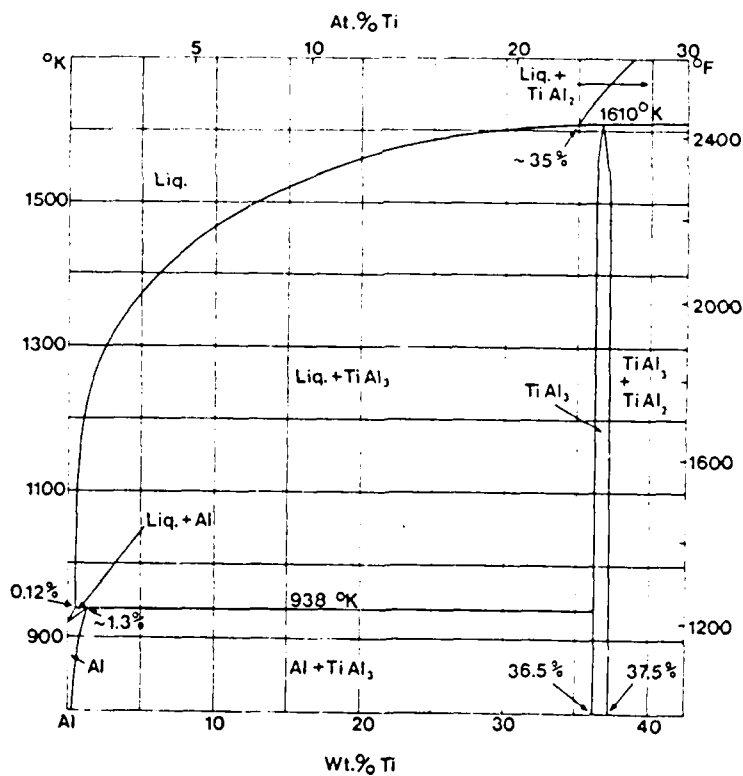
Figure 6. Metallographic cross sections of as-prepared Al - 8 Zr - 30 SiC (wt.%) composite filler metal powder particles. Magnification 500X.



Figure 7. Metallographic cross sections of as-prepared Al - 8 Ti- 30 SiC (wt.%) composite filler metal powder particles. Magnification 500X.



The aluminum end of the aluminum-zirconium equilibrium diagram



The aluminum end of the aluminum-titanium equilibrium diagram

Figure 8. Al-Zr and Al-Ti phase diagrams.

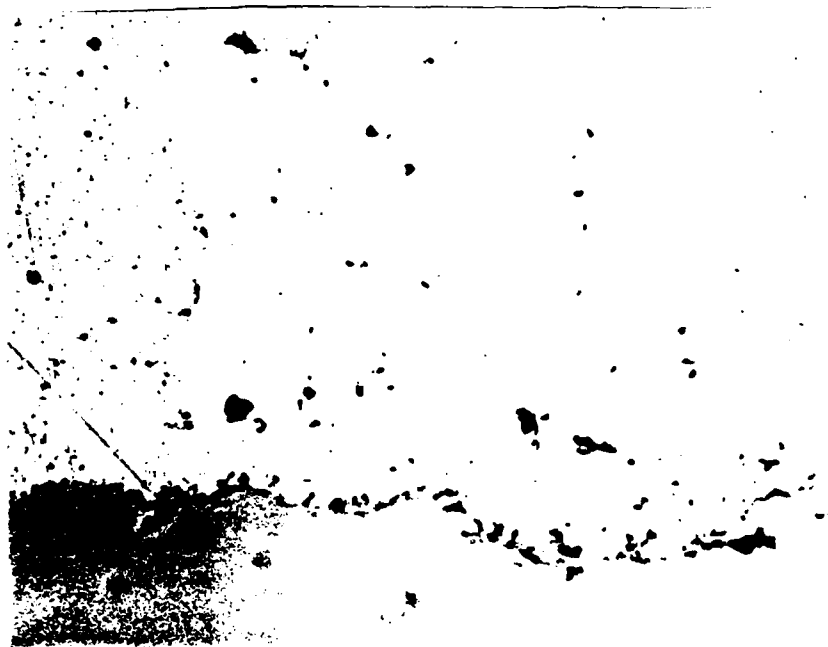


Figure 9. Low-pressure plasma deposited 1100 Al alloy coating. (500X).



Figure 10. Low-pressure plasma deposited 1100 Al - 30 wt.% SiC_p composite coating. (500X).

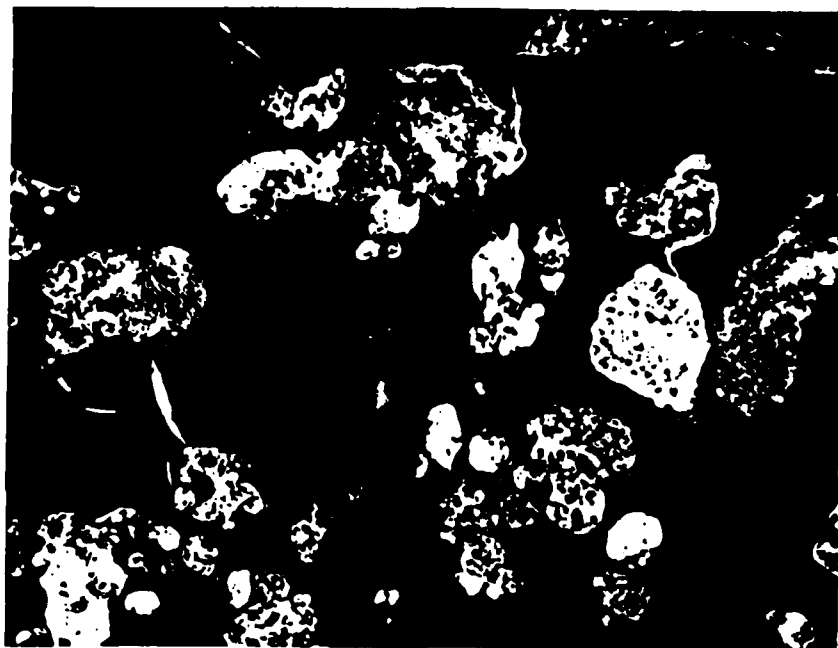


Figure 11. Oversprayed 1100 Al - 30 wt.% SiC_p composite powder. (500X).



Figure 12. Low-pressure plasma deposited Al - 3.0 wt.% Zr - 30 wt.% SiC_p composite coating. (500X).

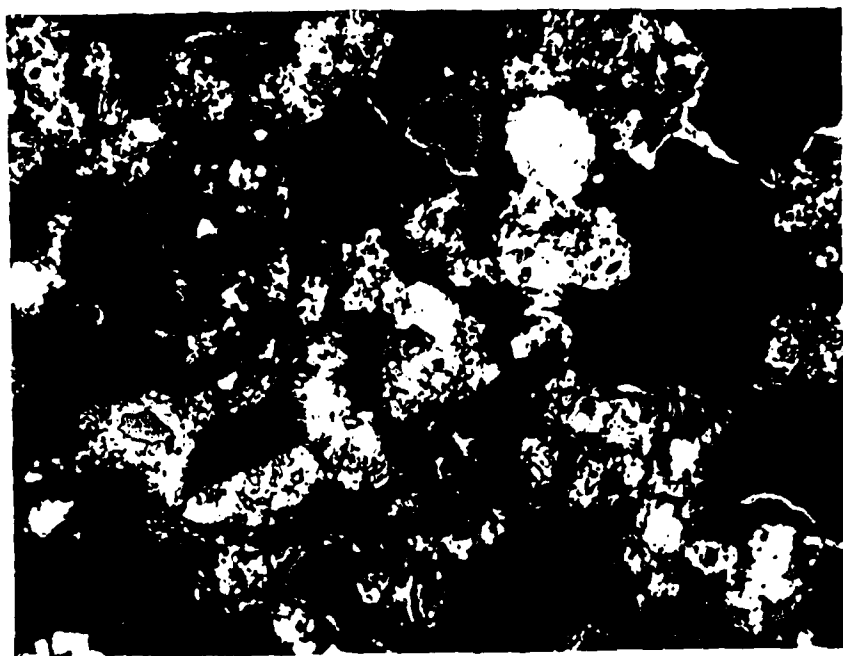


Figure 13. Oversprayed Al - 3.0 wt.% Zr - 30 wt.% SiC_p composite powder.
(500X).



Figure 14. Low-pressure plasma deposited Al - 5.0 wt.% Ti alloy coating.
(500X).



Figure 15. Low-pressure plasma deposited Al - 5.0 wt.% Ti - 30 wt.% SiC_p composite coating. (500X).



Figure 16. Oversprayed Al - 5.0 wt.% Ti - 30 wt.% SiC_p composite powder.
(500X).

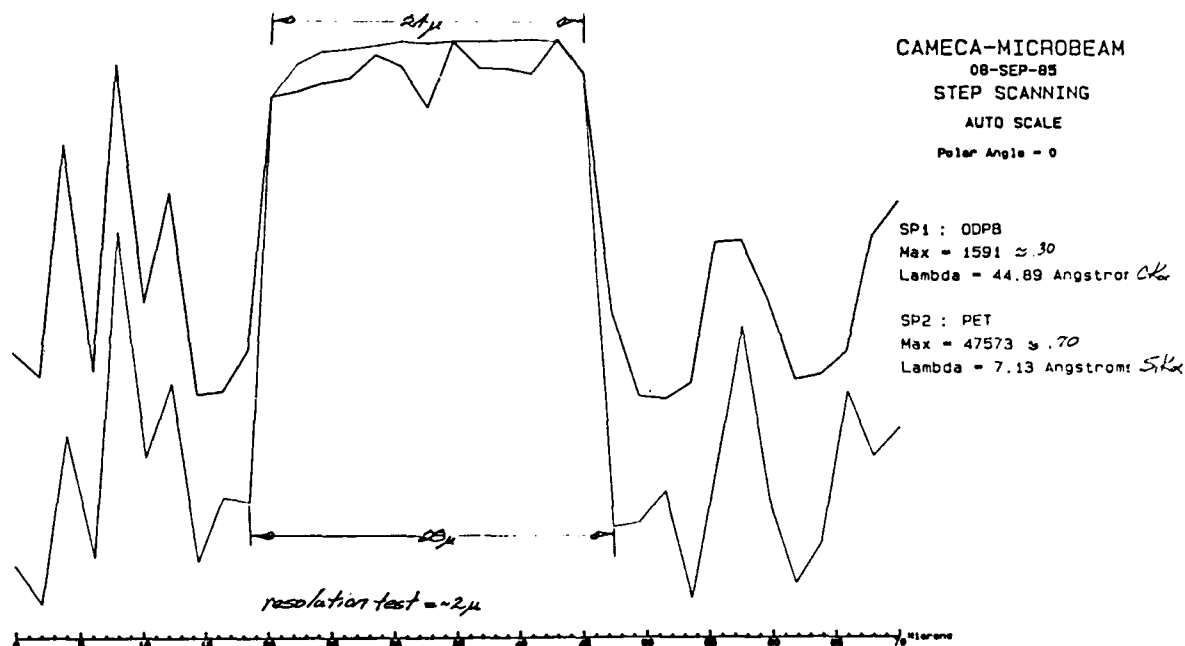


Figure 17. Microprobe trace across as-produced 1100 Al - 30SiC_p composite powder.

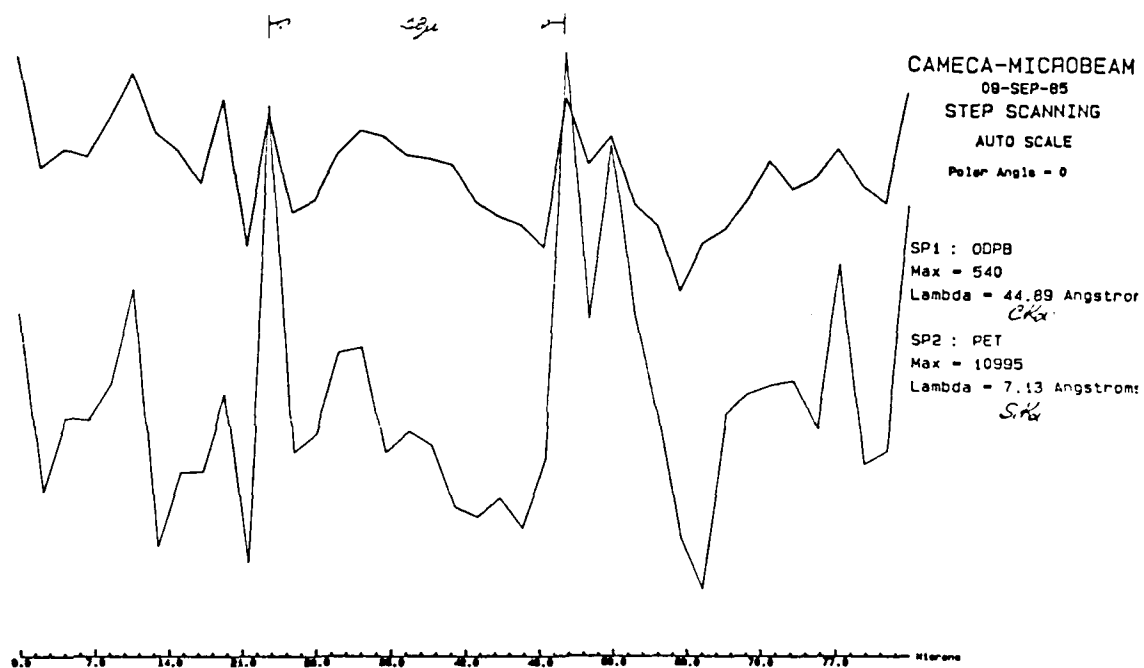


Figure 18. Microprobe trace across overspray 1100 Al - 30SiC_p composite powder.

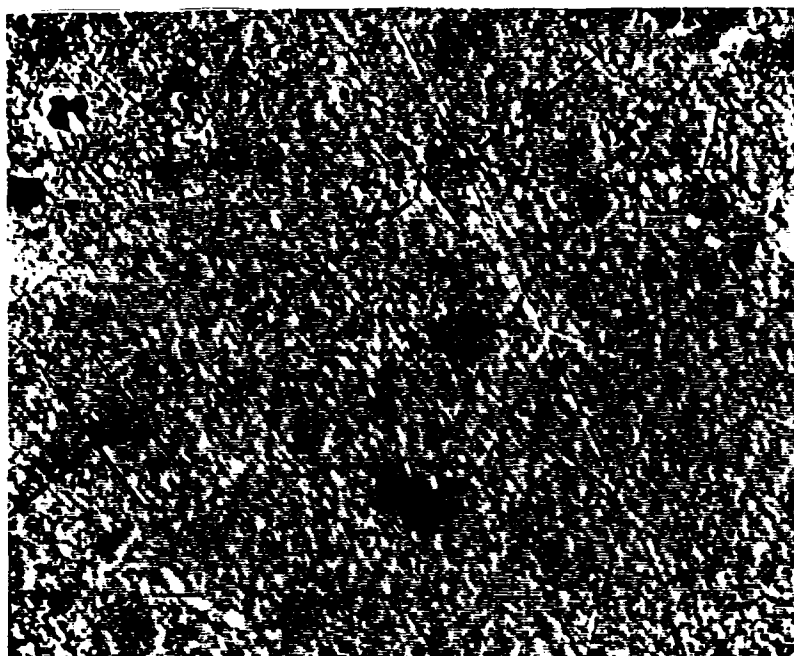


Figure 19. Backscattered electron image showing the path of the microprobe trace presented in Figure 18.

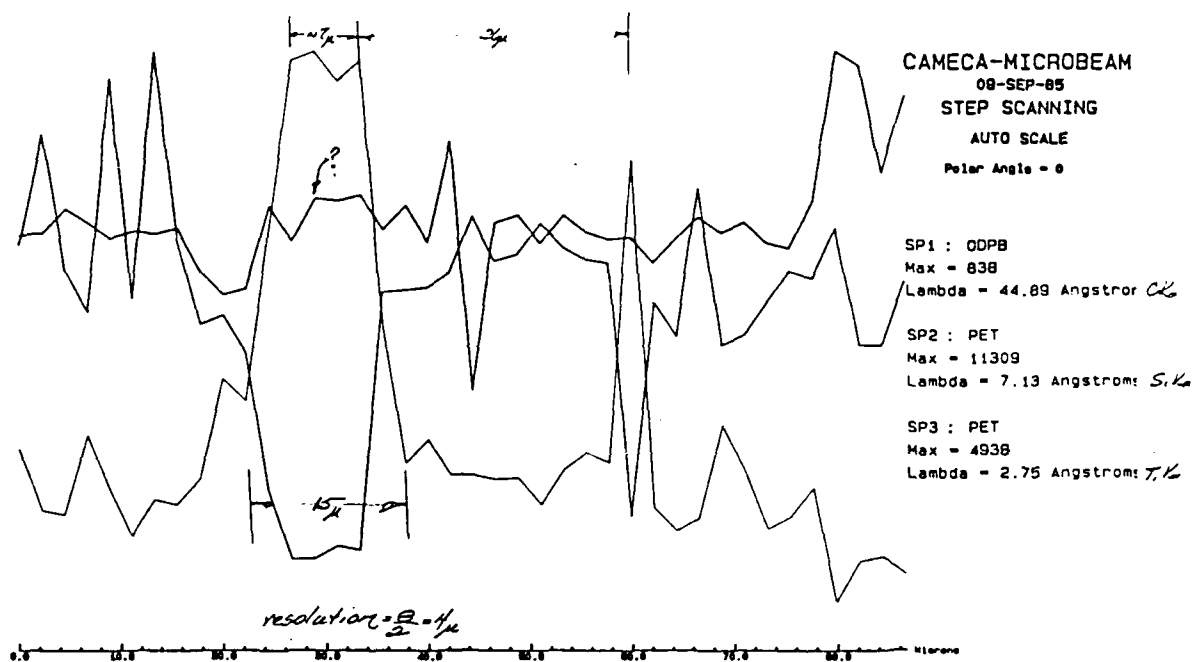


Figure 20. Microprobe trace across as-produced Al - 5Ti - 30SiC_p composite powder.



Figure 21. Backscattered electron image showing the path of the microprobe trace presented in Figure 20.

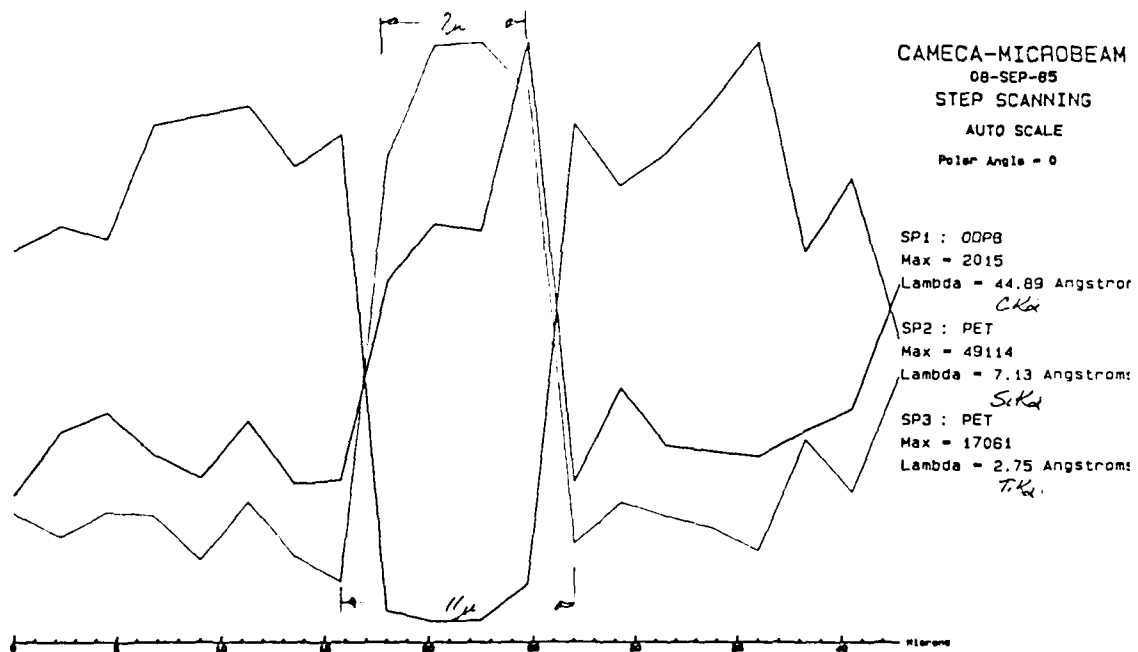


Figure 22. Microprobe trace across overspray Al - 5Ti - 30SiC_p composite powder.



Figure 23. Backscattered electron image showing the path of the microprobe trace presented in Figure 22.

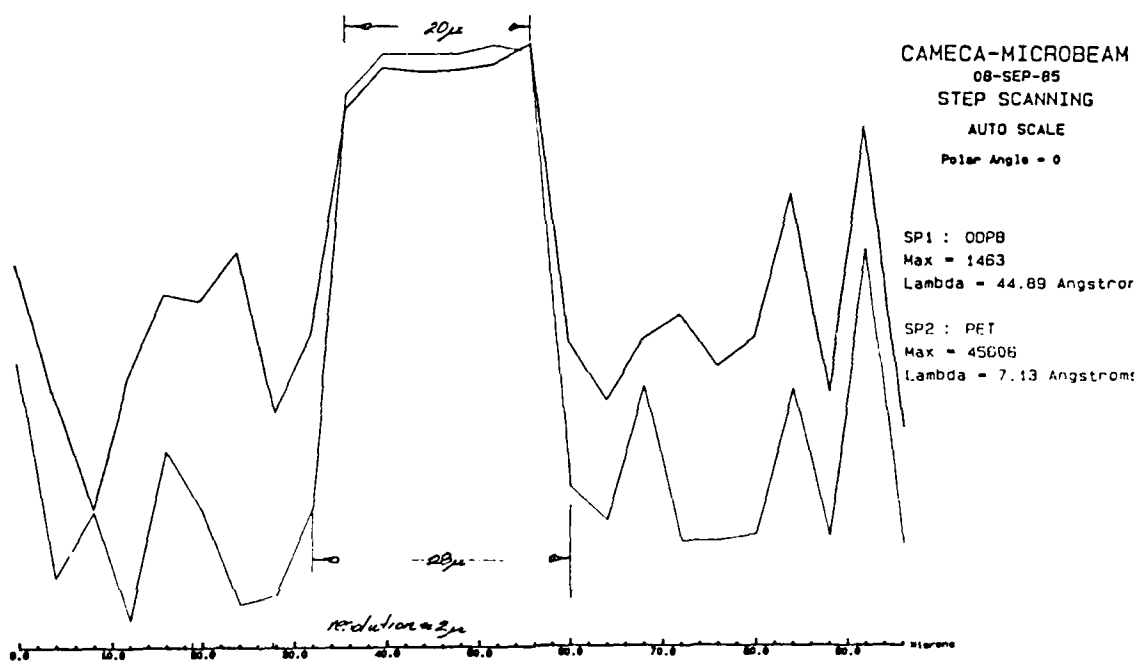


Figure 24. Microprobe trace across deposited 1100 Al - 30SiC_p coating.

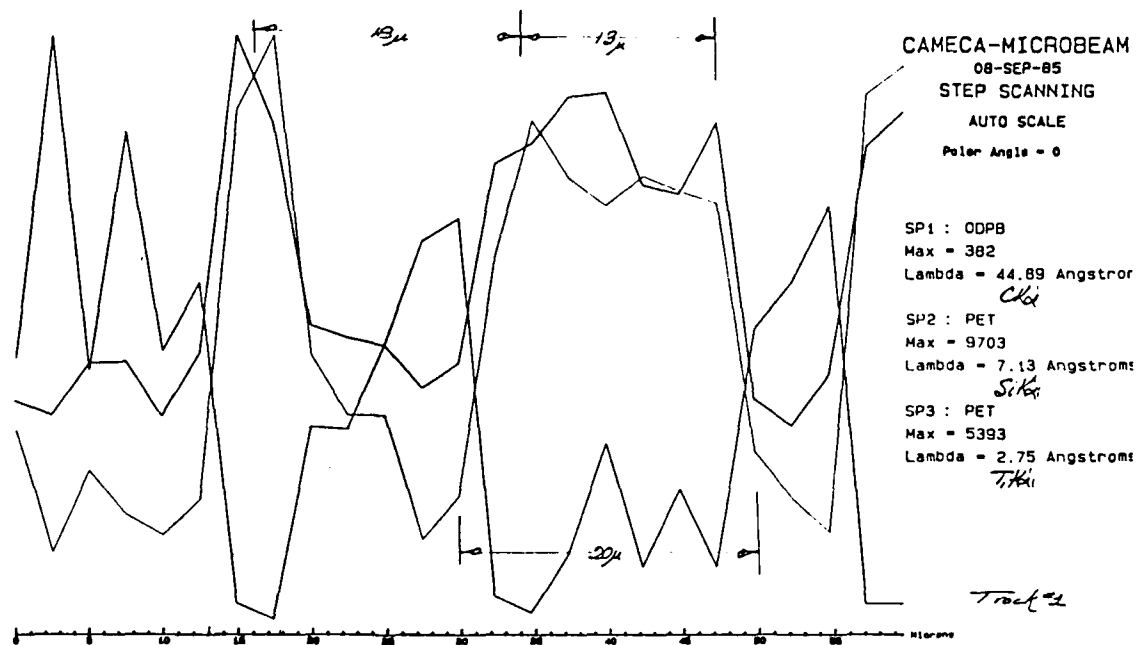


Figure 25. Microprobe trace across deposited Al - 5Ti - 30SiC_p coating.

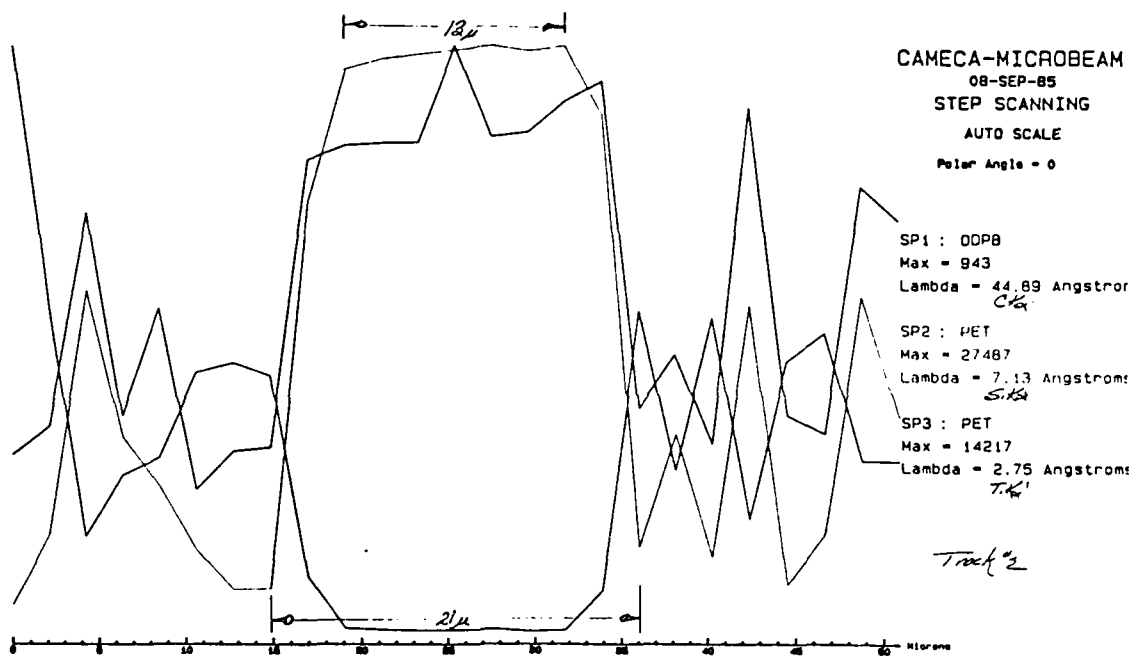


Figure 26. Microprobe trace across deposited Al - 5Ti - 30SiC_p coating.

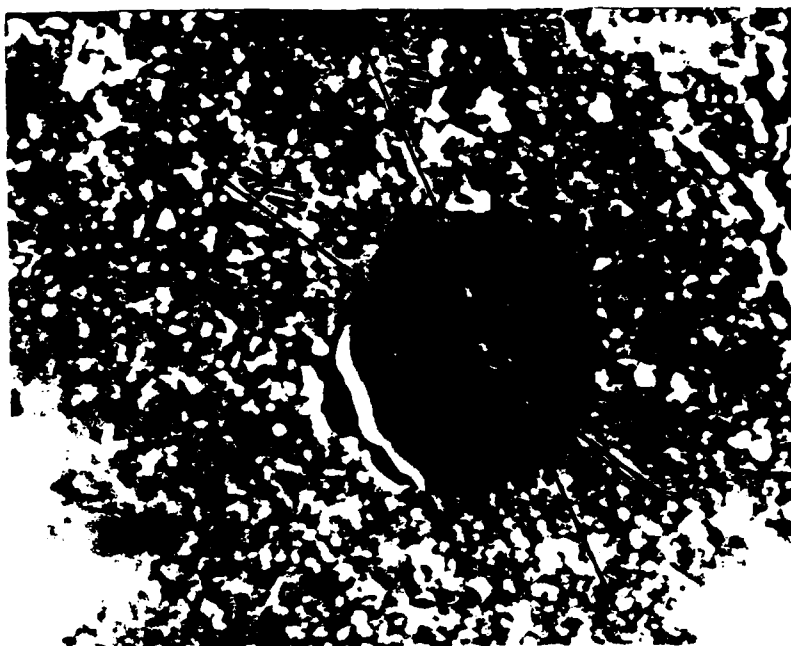


Figure 27. Backscattered electron image showing the path of the microprobe traces presented in Figures 25 and 26.

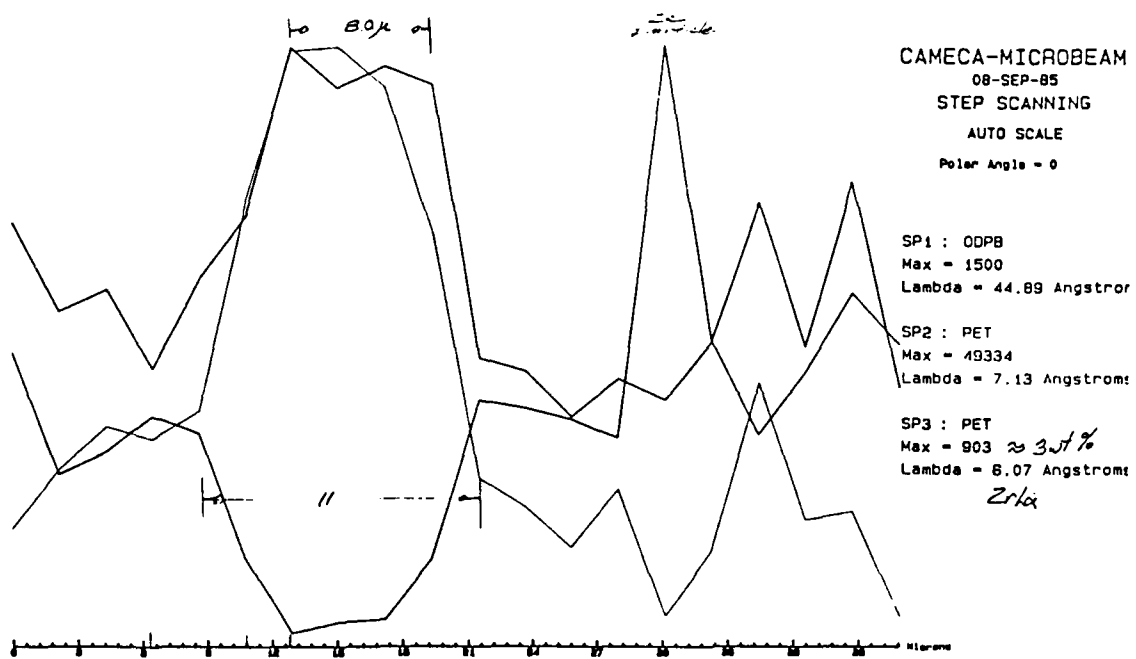


Figure 28. Microprobe trace across deposited Al - 3Zr - 30SiC_p coating.

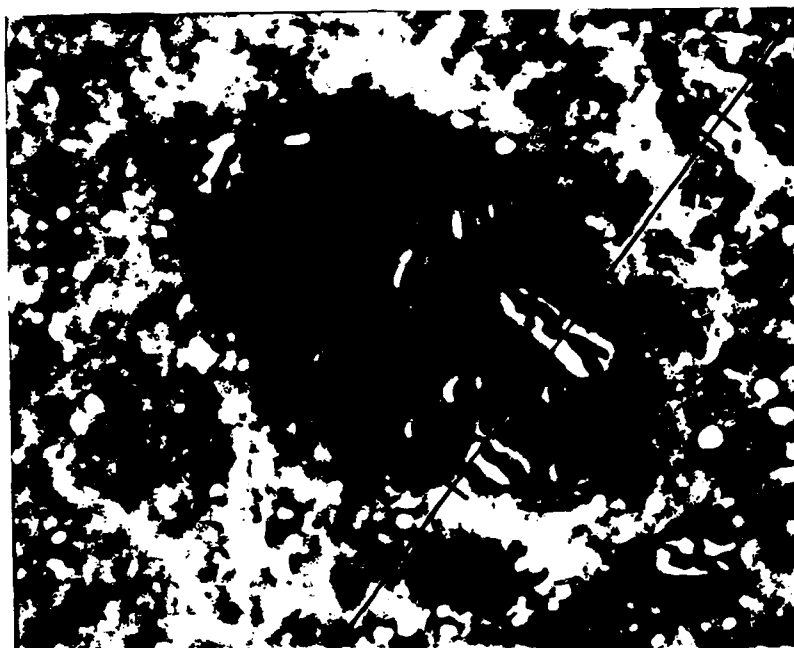


Figure 29. Backscattered electron image showing the path of the microprobe trace presented in Figure 28.

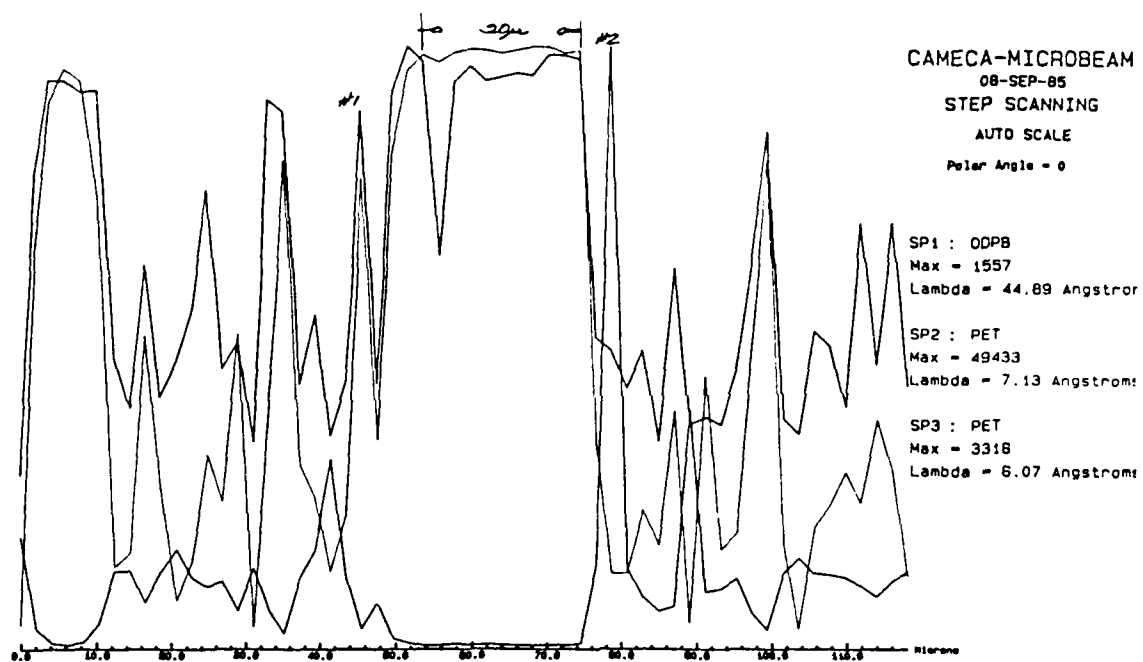


Figure 30. Microprobe trace across deposited Al - 32r - 30SiC_p coating.

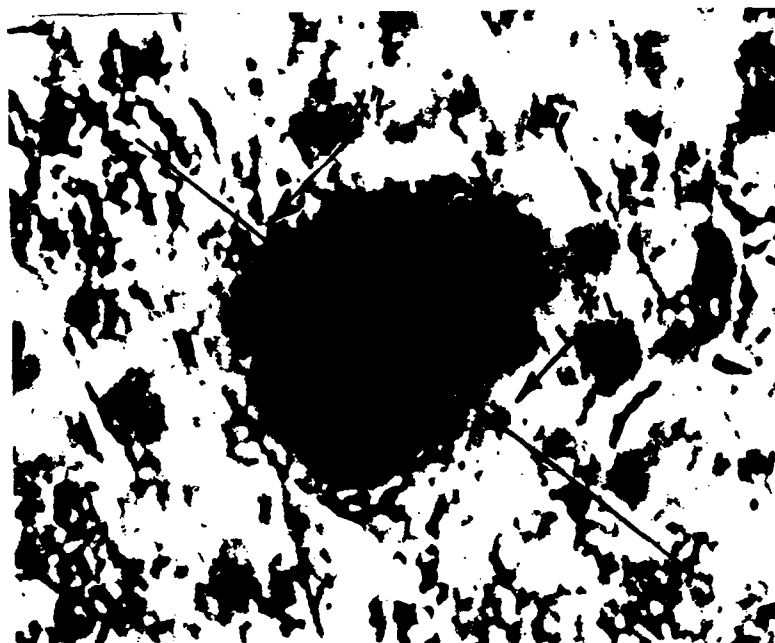


Figure 31. Backscattered electron image showing the path of the microprobe trace presented in Figure 30.

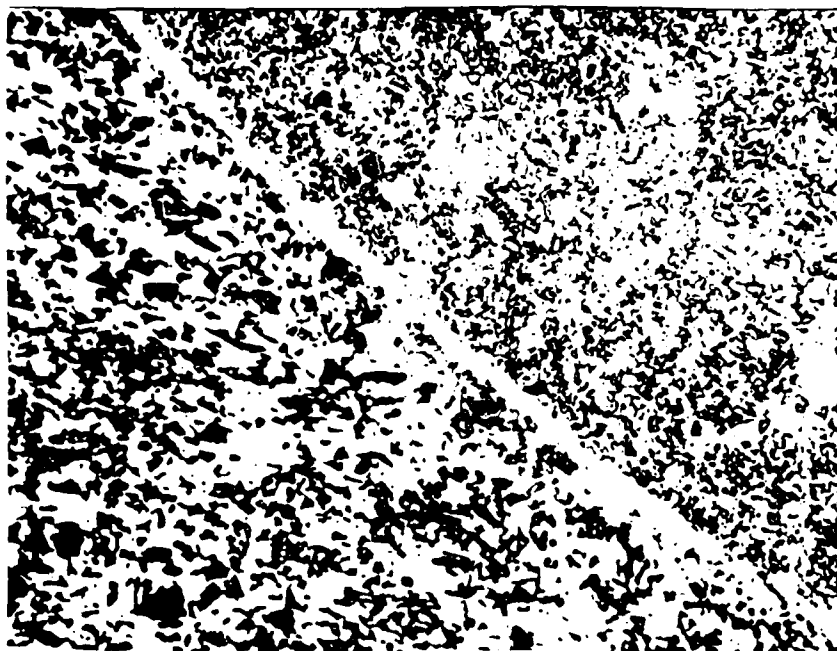


Figure 32. Optical micrograph of low pressure, transferred arc plasma weld produced using composite powder filler metals. Base metal (lower left) is 6061-30 wt.% SiC aluminum alloy. Weld metal (upper right) is 1100 aluminum -30 wt. % SiC. Fusion line extends from lower right to upper left. Note the metallurgical bond at the fusion line and the presence of an SiC-free zone at the fusion line. Magnification 500X.

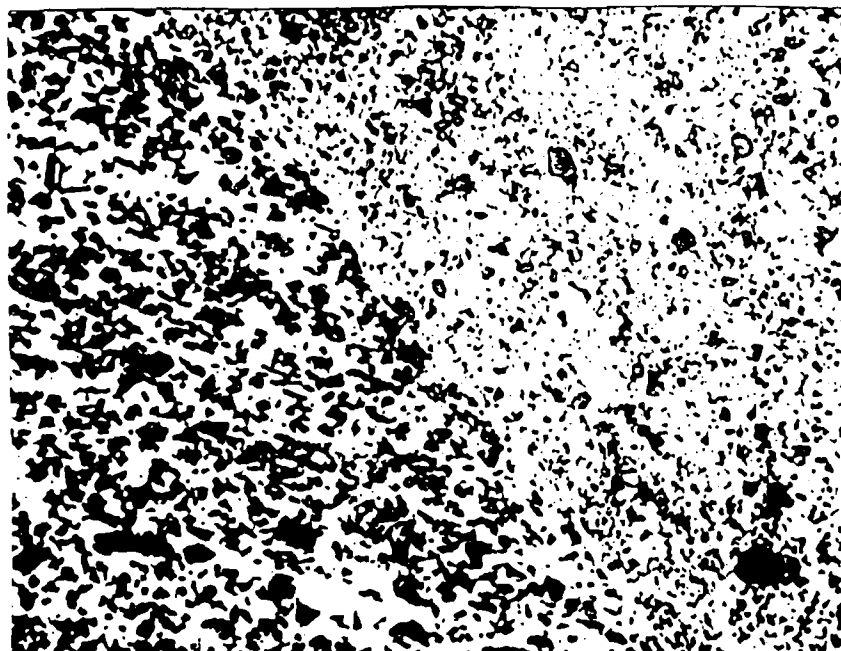


Figure 33. Optical micrograph of low pressure, transferred arc plasma weld produced using composite powder filler metals. Base metal (lower left) is 6061-30 wt.% SiC aluminum alloy. Weld metal (upper right) is aluminum - 5 wt.% titanium - 30 wt. % SiC. Fusion line extends from lower right to upper left. Note the metallurgical bond at the fusion line and the uniform distribution of SiC particulate phase both in the fusion line region and in the composite weld metal produced by this technique. Magnification 500X.

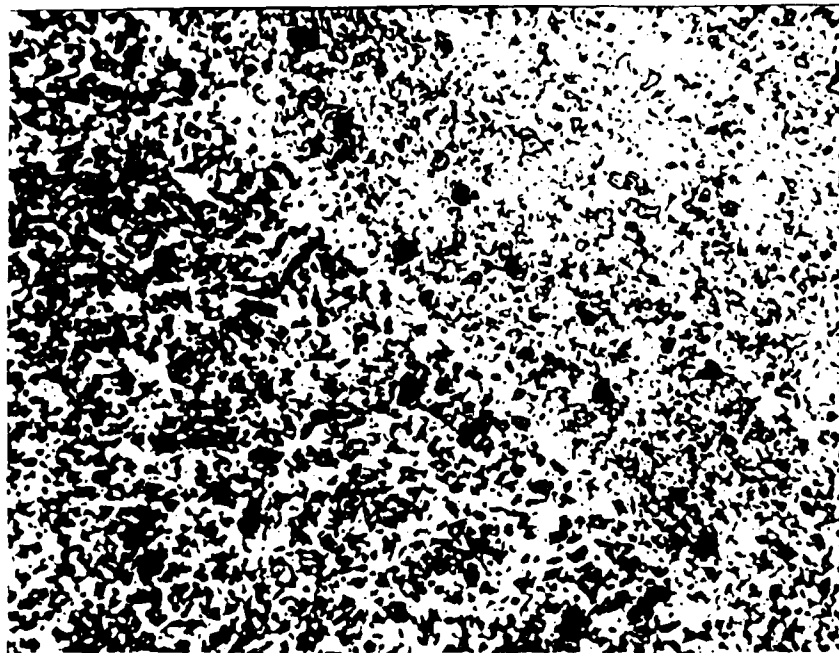


Figure 34. Optical micrograph of low pressure, transferred arc plasma weld produced using composite powder filler metals. Base metal (lower left) is 6061-30 wt.% SiC aluminum alloy. Weld metal (upper right) is aluminum - 3 wt.% zirconium - 30 wt. % SiC. Fusion line extends from lower right to upper left. Note the metallurgical bond at the fusion line and the uniform distribution of SiC particulate phase both in the fusion line region and in the composite weld metal produced by this technique. Magnification 500X.

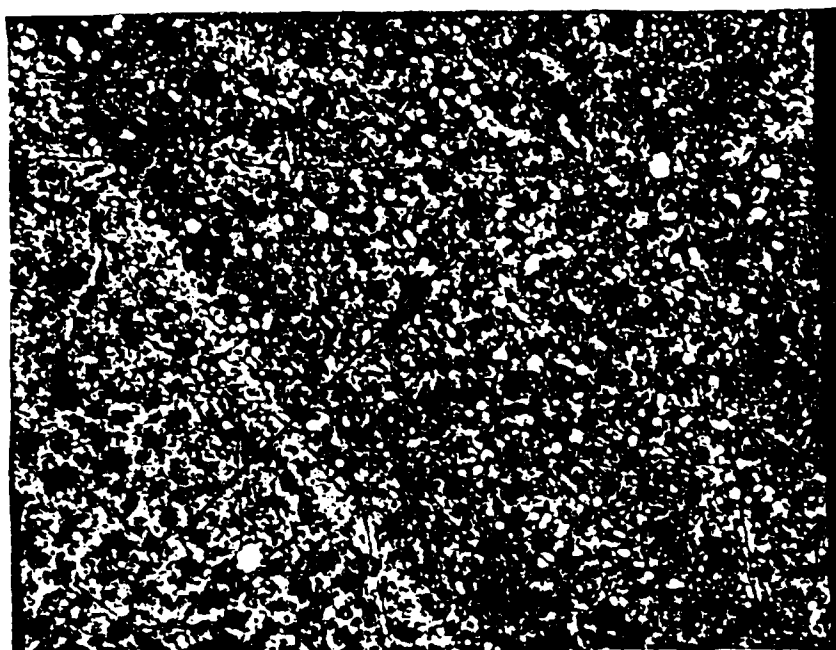


Figure 35. Fusion line and heat affected zone region of low pressure plasma deposited weld produced with 1100 aluminum - 30 wt. % SiC filler metal. Heat affected zone is at lower left, weld metal at upper right. Note band of lighter material which contains only very fine SiC particles along fusion line. Path of microprobe trace is shown. Backscattered electron image. Magnification 560X.

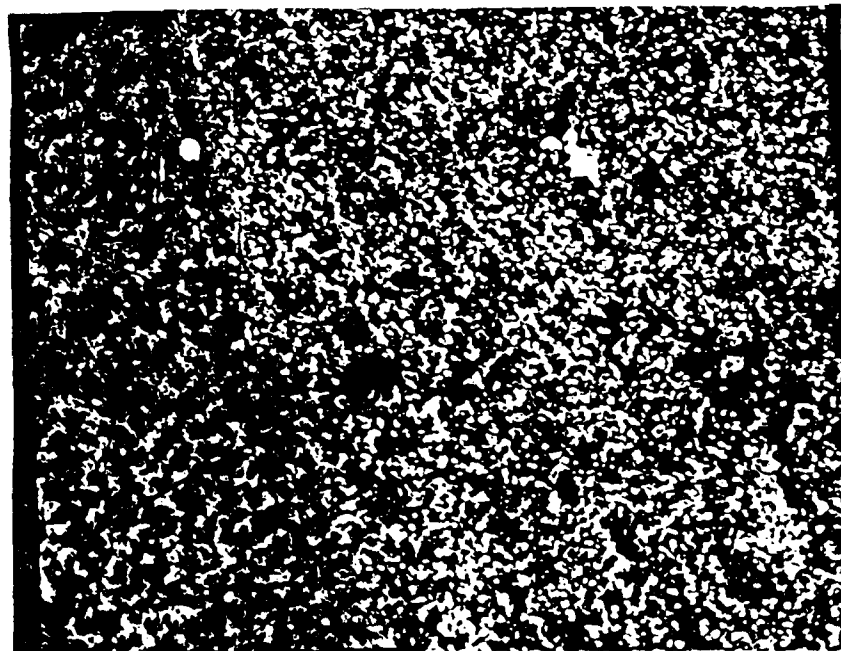


Figure 36. Fusion line and heat affected zone region of low pressure plasma deposited weld produced with aluminum - 3 wt. % Zr - 30 wt. % SiC_p filler metal. Heat affected zone is to the left, weld metal to the right. Note much narrower band of lighter material along fusion line when compared to Figure 1. Path of microprobe trace is shown. Backscattered electron image. Magnification 400X.

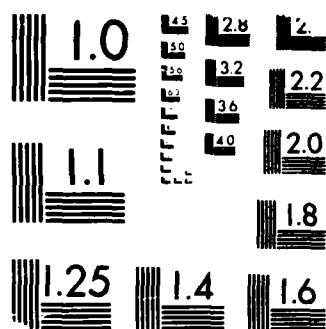
AD-A193 939

PLASMA JOINING OF METAL MATRIX COMPOSITES(U) HSNM INC 2/2
SAN MARCOS CA G H REYNOLDS ET AL 25 FEB 88
ARO-22817. 8-HS-5 DAAG29-85-C-0027

UNCLASSIFIED

F/G 11/6.2 NL





MICROCOPY RESOLUTION TEST CHART
 (NBS 1963-A)

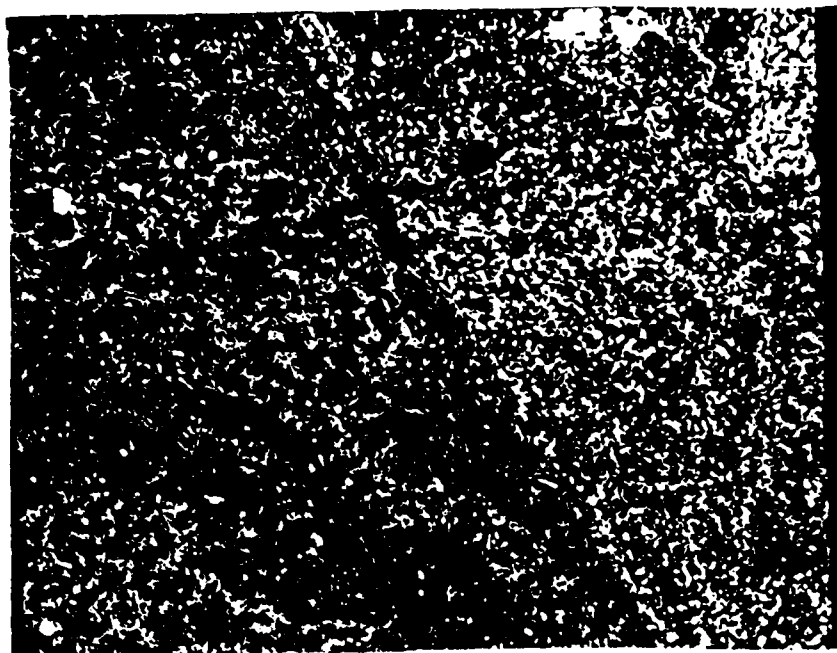


Figure 37. Fusion line and heat affected zone region of low pressure plasma deposited weld produced with aluminum - 5 wt. % Ti - 30 wt. % SiC_p filler metal. Heat affected zone is to the left, weld metal to the right. Note absence of lighter material along fusion line. Path of microprobe trace is shown. Backscattered electron image. Magnification 400X.

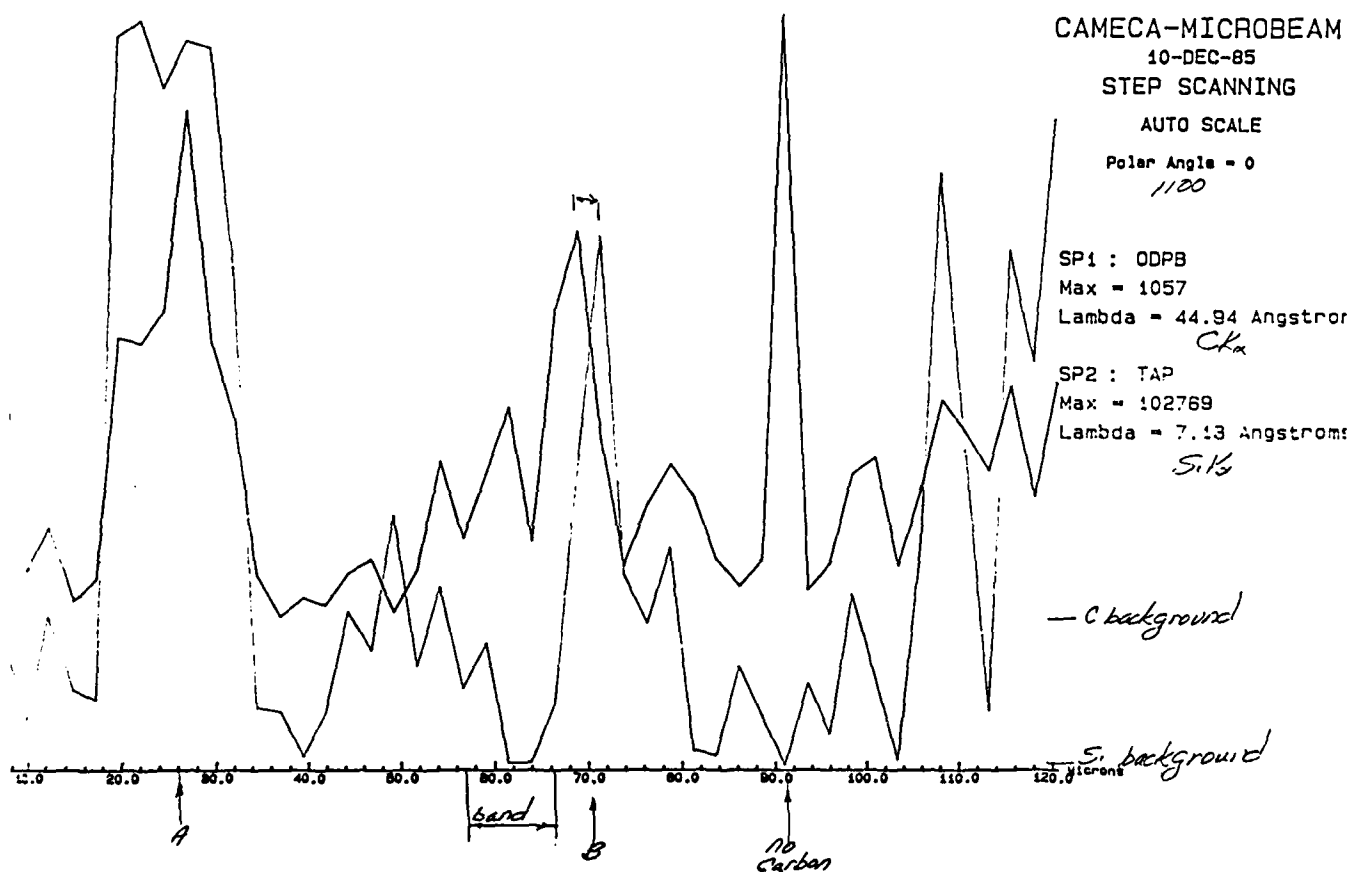


Figure 38. Electron beam microprobe traces for Si and C across heat affected zone, fusion line and weld metal. Path of microprobe trace shown in Figure 35.

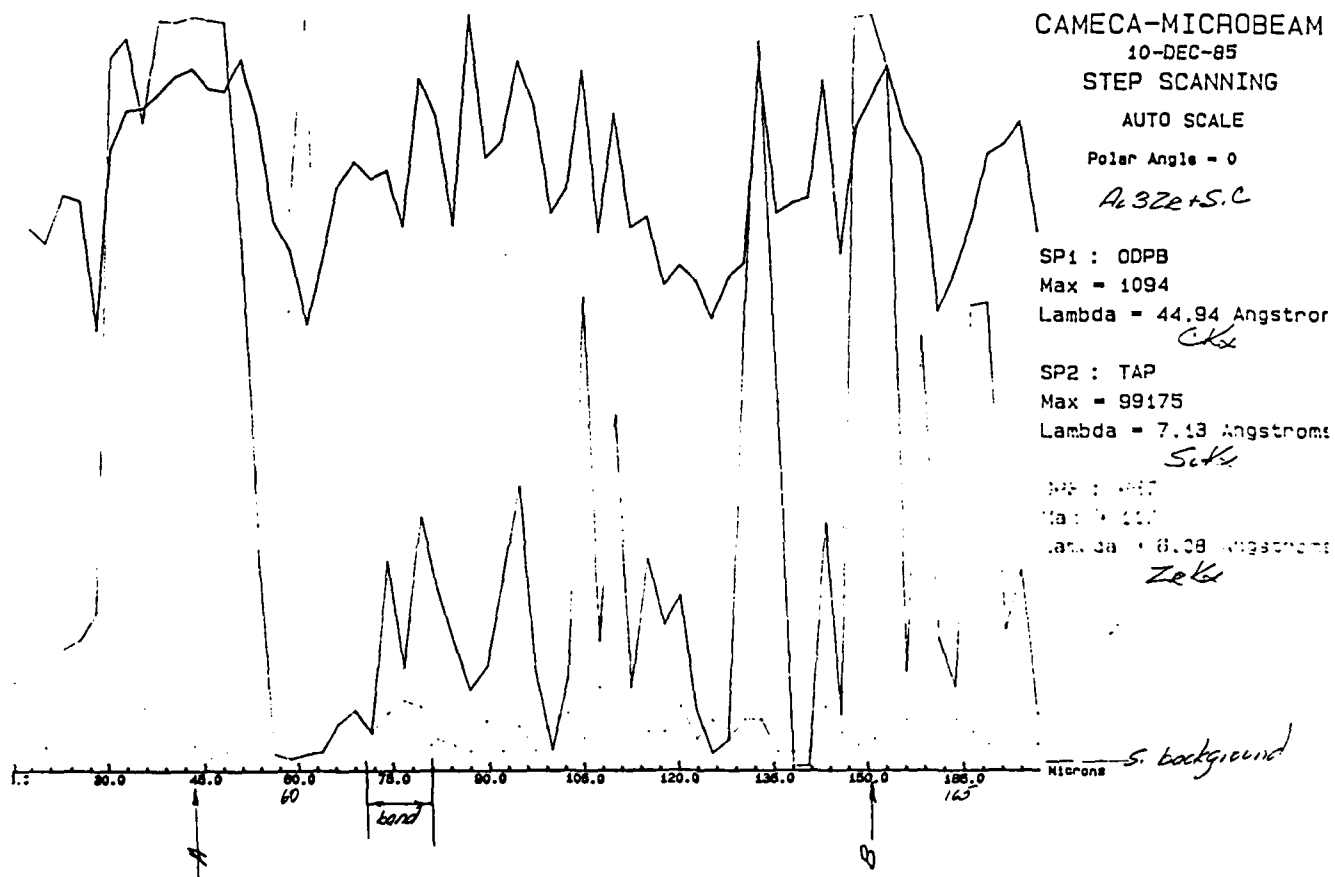


Figure 39. Electron beam microprobe traces for Si, C, and Zr across heat affected zone, fusion line and weld metal. Path of microprobe trace shown in Figure 36.

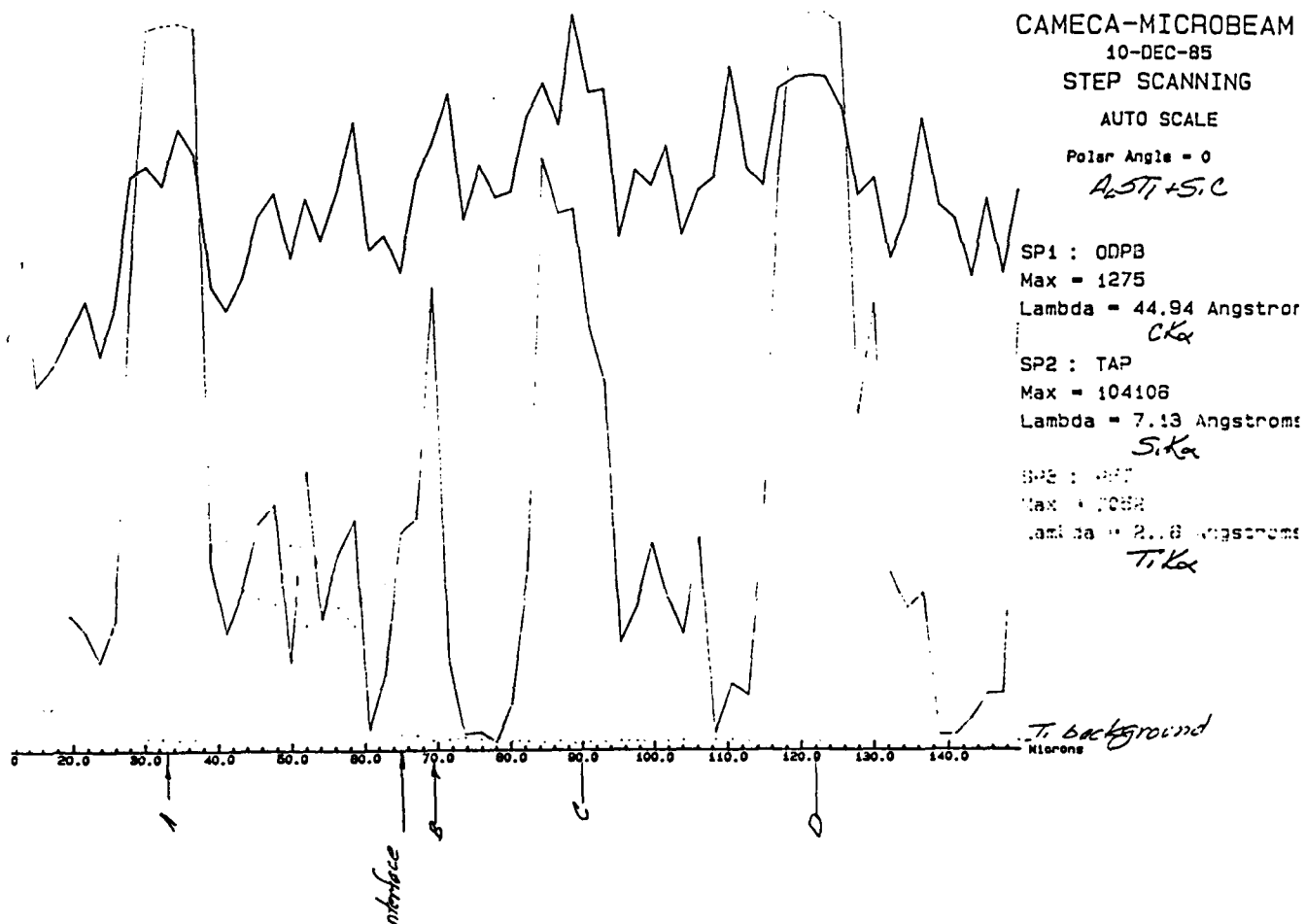


Figure 40. Electron beam microprobe traces for Si, C, and Ti across heat affected zone, fusion line and weld metal. Path of microprobe trace shown in Figure 37.

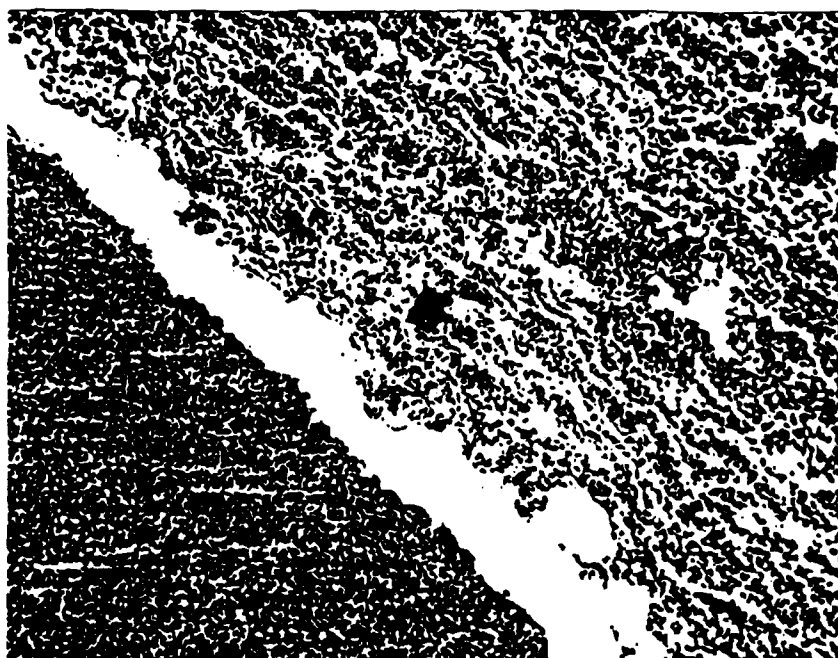
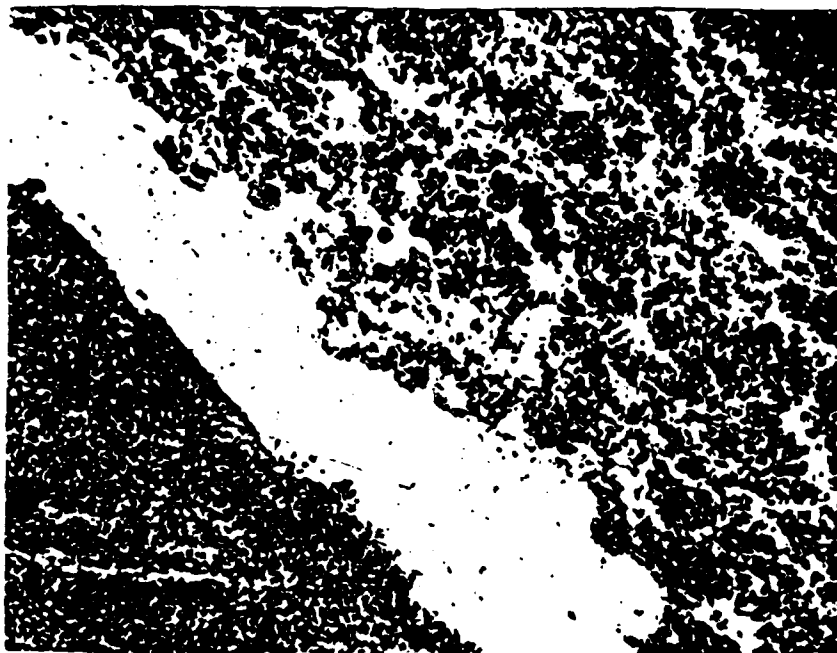


Figure 41. Fusion line microstructure of butt weld produced with Al - 8Zr - 30SiC_p composite filler metal. Top 500X, Bottom 200X.

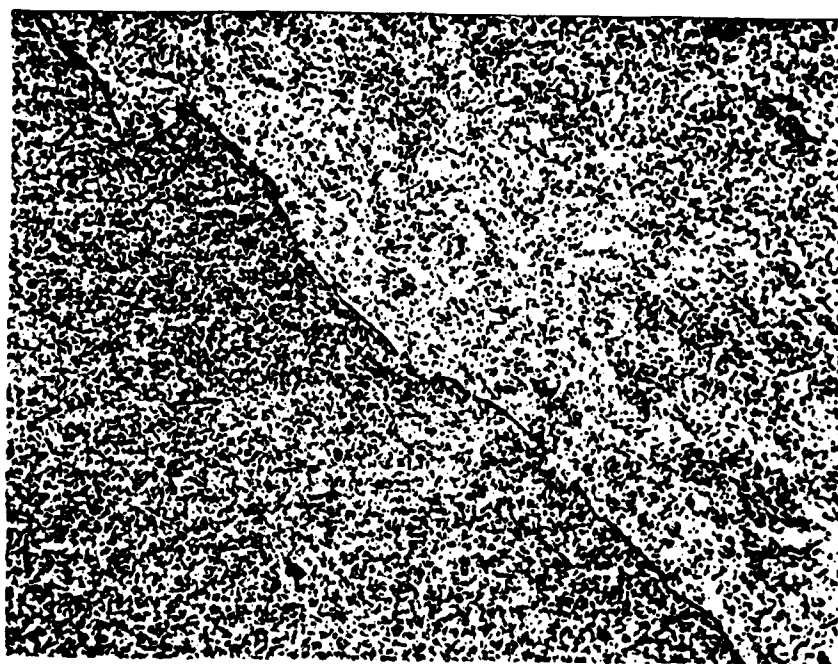
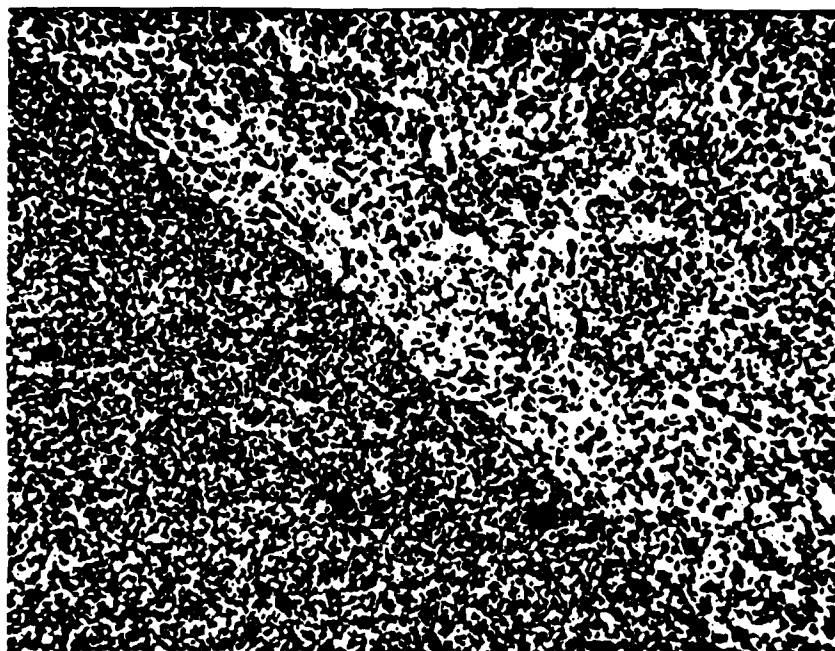


Figure 42. Fusion line microstructure of butt weld produced with Al - 8Ti - 30SiC_p composite filler metal. Top 500X, Bottom 200X.

END

DATE

FILMED

8-88

OTIC